J. Mech. Phys. Solids 206 (2026) 106353

Contents lists available at ScienceDirect

Journal of the Mechanics and Physics of Solids

journal homepage: www.elsevier.com/locate/jmps

Macro- and micro-mechanical perspectives on creep-fatigue interaction in Type 316L stainless steel

Fan Wu [a,*], Yang Liu [a], Huayue Zhang [a], Christos Skamniotis [b], Umer Masood Chaudry [a], Gareth Douglas [a], Joe Kelleher [c], Andrew Wisbey [d], Mike Spindler [e], Marc Chevalier [e], Bo Chen [f,*]

[a] School of Engineering, University of Leicester, Leicester LE1 7RH, UK
[b] Department of Engineering, King's College London, London, WC2R 2LS, UK
[c] ISIS Pulsed Neutron and Muon Source, STFC, Didcot OX11 0QX, UK
[d] Amentum, Birchwood Park, Warrington WA3 6GA, UK
[e] Nuclear R&D, EDF Energy, Barnwood, GL4 3RS, UK
[f] School of Engineering, University of Southampton, Southampton SO17 1BJ, UK

ARTICLE INFO

Keywords:
Creep-fatigue interaction
Asymmetric load waveform
Neutron diffraction
Lattice strain
Crystal plasticity modelling
Deformation
Austenitic steels

ABSTRACT

Creep-fatigue of Type 316L stainless steel under asymmetric waveforms (specifically slow tension-fast compression, S-F, and fast tension-slow compression, F-S) has been understudied, despite its significant implications as demonstrated in this work. This study bridges macro- and micro-mechanical perspectives through a combined approach, involving high-temperature testing, scanning electron microscopy, X-ray computed tomography, neutron diffraction, and crystal plasticity modelling. Macro-mechanical tests revealed distinct deformation behaviours under S-F and F-S waveforms with and without a 1-hour tensile dwell at 550 °C, with S-F reducing lifespan in both fatigue and creep-fatigue conditions. Post-mortem analyses revealed distinct fracture morphologies induced by tensile dwell, with creep-fatigue S-F specimen exhibiting more pronounced intergranular-dominant fracture and higher internal defect volume. It also exhibited the highest number fraction of medium-sized (10–40 μm) microcracks, which correlates with its shortest fatigue life and more creep damage accumulation. Higher grain-level deformation incompatibility was observed during tensile dwell in the S-F load waveform. Crystal plasticity modelling revealed that the higher tensile stress amplitudes during S-F loading stem from increased dislocation density, with average densities at peak tensile strain during the saturation cycle reaching 186 μm^{-2} for S-F and 147 μm^{-2} for F-S waveforms. These findings establish a strong link between macroscopic and microscopic behaviours under asymmetric loading, emphasising the potential of S-F waveforms for cost-effective creep-fatigue experiment design. Furthermore, for the asymmetric waveforms studied, creep-fatigue life assessment using the ductility exhaustion method demonstrates greater accuracy than those based on the time fraction method.

* Corresponding authors.
E-mail addresses: fw.leicester@outlook.com (F. Wu), b.chen@soton.ac.uk (B. Chen).

https://doi.org/10.1016/j.jmps.2025.106353
Received 14 June 2025; Received in revised form 5 September 2025; Accepted 7 September 2025
Available online 8 September 2025

1. Introduction

Creep-fatigue interaction is a primary failure mode in superheater components used in high-temperature nuclear plants (Prasad Reddy et al., 2015b; Wang et al., 2019; Wen et al., 2017). The interplay between creep and fatigue significantly limits the material's lifespan (Anahid et al., 2011; Goodall et al., 1981; Li et al., 2017). Therefore, an improved understanding of how the material responds to various creep-fatigue loading scenarios is essential for the high-temperature structural integrity assessment. Considerable experimental efforts have been dedicated to testing the isothermal creep-fatigue behaviour of austenitic stainless steels, particularly Type 316 and its variants (316H, 316L, 316L(N), etc.) as well as Type 304 stainless steels. Various factors such as strain range (Spindler, 2018; Yamaguchi and Kanazawa, 1980), strain rate (Xie et al., 2019; Yamaguchi and Kanazawa, 1980), peak dwell (Bhanu Sankara Rao et al., 1993; Hormozi et al., 2015; Sauzay et al., 2004; Takahashi et al., 2008), and load waveform (Lee et al., 1991; Okazaki et al., 1984; Yamaguchi and Kanazawa, 1980) have been found to significantly influence the creep-fatigue. A detailed summary is elaborated below.

In terms of total strain range, our general understanding is that fatigue life is negatively correlated with its magnitude. For example, at a fixed strain rate of 6.7×10^{-3} /s, the fatigue life of 316L stainless steel at 600 ℃ increased from 450 to 7000 cycles as the strain range decreased from 2.0 % to 0.6 % (Yamaguchi and Kanazawa, 1980). The same trend was observed on 316H stainless steel, where at test condition of 550 ℃ and strain rate of 2.5×10^{-4} /s, the increased strain range from 0.6 % to 1.2 % reduced the fatigue life by a factor of four (Spindler, 2018). In terms of strain rate, a longer fatigue life is associated with the higher rate. At 1.2 % strain range, a doubling of the fatigue life of 316L stainless steel at 650 ℃ was found with the increase of strain rate from 5×10^{-4} /s to 5×10^{-3} /s (Xie et al., 2019). Similarly, at a higher strain range of 2.0 %, one order of magnitude faster rate resulted in a threefold increase in fatigue life of 316H stainless steel (Yamaguchi and Kanazawa, 1980). In terms of peak dwell, a 1-hour tensile dwell per cycle can reduce the fatigue life at 550 °C of 316L and 316L(N) stainless steels by more than half (Sauzay et al., 2004; Takahashi et al., 2008). In addition, Bhanu Sankara Rao et al. (1993) observed that compared to the tensile dwell, neither the compressive nor the combined tensile and compressive hold caused fatigue life reduction in 304 stainless steel.

An important but underexplored factor in load waveform is the asymmetric waveshape, which is typically implemented using fast and slow strain rates of approximately 10^{-3} /s and 10^{-5} /s, respectively. To demonstrate the significance of this loading condition, the effects of asymmetric waveforms on fatigue life are compared with existing literature data in the Discussion section (Fig. 12), revealing their positioning within the broader context of creep-fatigue behaviour. Yamaguchi and Kanazawa (1980) conducted pioneering work on 316L stainless steel, revealing that a slow tension-fast compression (S-F) waveshape reduced fatigue life by 75 % than its symmetric counterpart, both tested at 2.0 % strain range. A similar trend was found on 304 stainless steel, where a S-F waveshape reduced the fatigue life to 22 % of that under symmetric loading (Lee et al., 1991). It is worth noting that the level of fatigue-life reduction with an S-F waveshape is similar to the effect of incorporating a 60-minute strain controlled tensile dwell in a creep-fatigue test using symmetric waveform (Yamaguchi and Kanazawa, 1980). A question arises as to what causes such significant difference between asymmetric and symmetric load waveforms. Answering this question could unlock opportunities for designing more cost-efficient creep-fatigue tests by reducing test durations. Taking the work in Yamaguchi and Kanazawa (1980) as an example, at a total strain amplitude of 1.2 %, achieving a similar number of cycles to failure required 1.3 days with an S-F waveform, whereas it took 25.8 days with a 60-minute tensile hold under symmetric loading. This remarkable time difference occurs because the slow tension phase in S-F waveform is substantially shorter than the extended tensile hold while producing comparable damage. Beyond practical applications, a deeper understanding can help identify key factors controlling creep cavitation mechanisms during creep-fatigue.

In fact, there are only two experimental studies and one modelling work that sought to establish the mechanistic understanding of asymmetric load waveform on creep-fatigue. Okazaki et al. (1984) studied the effect of one cycle of S-F waveform on the fatigue crack growth of 304 stainless steel at 600℃. They concluded that the formation of a creep damage region (wedge cracks) at the crack tip during the S-F cycle was the root cause of the accelerated crack propagation. Yamaguchi and Kanazawa (1980) attributed the reduced fatigue life of 316 stainless steel under a multi-cycle asymmetric waveform to wedge and cavity-type cracks. Hu et al. studied the role of asymmetric load waveforms, both one-cycle (Hu et al., 2021) and multi-cycle (Hu et al., 2022), on cavitation damage of 316 stainless steel, through theoretical modelling of cavitation process. One main finding was the distinct difference between one-cycle and multi-cycle S-F load waveforms and their reversed order (i.e., fast tension-slow compression, abbreviated as F-S).

This discrepancy motivated us to conduct four systematic tests (fatigue S-F and F-S, compared with creep-fatigue S-F and F-S) to understand the macro-mechanical perspective. Given the intergranular nature of cavitation damage, understanding the micro-mechanical perspective of the asymmetric waveform is crucial for interpreting the macro-mechanical data. As a result, neutron diffraction experiments, coupled with crystal plasticity modelling, were also employed. Before presenting our research findings, we provide a brief review of the state-of-the-art knowledge on deformation mechanisms related to creep, fatigue and creep-fatigue.

Under strain-controlled cyclic loading, austenitic stainless steel exhibits three characteristic stages: hardening, saturation, and softening (Hu et al., 2023; Hyde et al., 2010; Srinivasan et al., 1999; Xie et al., 2019). At 550 °C and strain rate of 3×10^{-3} /s, the tensile stress amplitude in the saturation stage of 316L(N) stainless steel increased from 235 MPa to 345 MPa as the strain range increased from ± 0.3 % to ± 0.6 % (Sauzay et al., 2004). Additionally, at 600 ℃ and under a strain amplitude of ± 0.6 %, the stress amplitude was 360 MPa at a higher strain rate of 3×10^{-3} /s, which is higher than 335 MPa obtained at a lower rate of 3×10^{-5} /s (Prasad Reddy et al., 2015a). The effect of tensile dwell on tensile stress amplitude was dependent on the dwell time (Liang et al., 2023). Specifically, a 30-second dwell increased the stress amplitude of 316L stainless steel by 15 MPa, but a 300-second dwell decreased it by 20 MPa, compared to the pure fatigue test. Similarly, in tests with a strain amplitude of ± 0.4 % and a strain rate of 1×10^{-3} /s, 30-second and 300-second tensile holds increased and decreased the stress during the saturation stage by 15 MPa and 20 MPa, respectively, compared to zero hold. The complexity increased when considering the roles of tensile, compressive, or combined holds

(Bhanu Sankara Rao et al., 1993).

Performing additional creep-fatigue tests alone is unlikely to elucidate the mechanisms, highlighting the need to collect data from a micro-mechanical perspective. Synchrotron X-ray and neutron diffraction, combined with high-temperature loading (e.g., tension (Wang et al., 2018), creep (Chen et al., 2015a; Mamun et al., 2019b), creep-fatigue (Li et al., 2021; Mamun et al., 2019a, 2020) on 316 stainless steel, are established methods to gather the information at the grain family level. For example, upon creep loading to the test stress of 155 MPa at 650 °C, the lattice strain of the {200} grain family was 1700 microstrains (which is $\varepsilon \times 10^{-6}$). This strain increased by 250 microstrains over the initial 1-hour creep and then showed no change in the next 2 h. In contrast, a 1- to 3-hour compressive hold at 155 to 170 MPa did not cause any measurable change in the lattice strain (Li et al., 2021). Li et al. (2021) compared the lattice strain of the {200} grain family after a stress transition from 155 MPa to −155 MPa, followed by a 2-hour compressive hold, prior to reversing back to 155 MPa. They found that the lattice strain reduced by about 500 microstrains compared to its value prior to compression. Mamun et al. (2019a) observed a synchronous evolution of creep strain in the bulk sample and the lattice strain as measured from the {200} grain family during the compressive hold. In addition, nearly all previous neutron diffraction studies on 316 stainless steels (e.g., Chen et al., 2015b; Clausen et al., 1998; Daymond and Bouchard, 2006; Peng et al., 2002; Pokharel et al., 2019; Rao et al., 2012) focused on four major grain families of {200}, {220}, {111} and {311}. This is because {111} shows the highest peak intensity, {311} is the orientation least affected by intergranular strains (representing the bulk behaviour), while {200} and {220} represent the most compliant and stiffest grain orientations, respectively.

To the best of our knowledge, no studies have been conducted on the asymmetric waveform of creep-fatigue from a micro-mechanical perspective. By performing both the macro- and micro-mechanical experiments, we fill this knowledge gap of the interplay between creep and fatigue under asymmetric creep-fatigue waveforms. Crystal plasticity modelling was also undertaken to enhance confidence in the new findings by combining the measured and predicted macroscopic behaviour and internal state evolution. Finally, the paper considers knowledge translation by utilising the high-temperature structural integrity approach (i.e., creep-fatigue interaction diagram (Ainsworth, 2006)) to evaluate the asymmetric waveform data in comparison with data generated using symmetric loading.

2. Experimental procedures

2.1. Material

Type 316L stainless steel, provided by EDF Energy, has a nominal composition of 0.023C, 1.74Mn, 0.41Si, 0.023P, 0.001S, 16.89Cr, 11.72Ni, 2.56Mo, 0.20Cu, 0.002Ti, 0.077N (all in wt. %), with Fe as the balance. The 316L stainless steel used in this study was subjected to a solution annealing treatment at 1050 °C for 1 h and 15 min, followed by water quenching. The average grain size was measured to be 50 ± 8 μm, using both the electron backscattered diffraction (EBSD) technique (refer to Fig. S1a) and linear intercept method.

2.2. Fatigue and creep-fatigue testing with an asymmetric waveform

A total of four fatigue and creep-fatigue tests were conducted on a servo-electric test frame to examine the macro-mechanical behaviour of Type 316L stainless steel at 550 °C. These tests are named as fatigue S-F, fatigue F-S, creep-fatigue S-F, and creep-fatigue F-S, where the abbreviations of S-F and F-S indicate that the specimen was subjected to a slow tension-fast compression type asymmetric waveform, and vice versa. The test procedure followed BS 7270:2006 (2006). Specimen dimensions are shown in Fig. S2a.

For all tests, continuous cycling was conducted under strain control, while the creep was conducted under stress control. The total strain amplitude was ± 0.6 %, with the fast strain rate fixed at 3×10^{-3} /s and the slow strain rate fixed at 3×10^{-5} /s. The four load waveforms are shown schematically in Fig. S3. Testing was terminated upon reaching N_{25}, defined by the number of cycles for peak tensile stress to decrease by 25 % from the saturation stage. Macroscopic stress and strain measurements on the test specimen, using calibrated load cell and high-temperature extensometer, respectively, were recorded at defined intervals based on the following criteria: every 60 s, every 0.2 kN force change, or every 1 μm displacement, whichever came first. Each test specimen was initially heated to 550 °C, and the temperature fluctuations were maintained within ± 3 °C throughout the test.

Given the uncommon asymmetric load waveforms, trial tests were conducted on 304 stainless steel under the same test conditions to ensure the reliability of the test machine and controller. These validation experiments covered both fatigue and creep-fatigue S-F conditions to confirm waveform control stability and experimental repeatability. The results demonstrated high repeatability and were found to be in good agreement with reference (Sauzay et al., 2004). Further details, including hysteresis loops and peak stress evolution, are provided in Fig. S4 of the Supplementary Material.

2.3. Post-mortem characterisation

Post-mortem examination was conducted using fractography and X-ray computed tomography (XCT). Fractography analysis was performed with an FEI Quanta 650 scanning electron microscope (SEM) under secondary electron imaging mode at 20 keV. For detailed characterisation of the damage process, a ZEISS Xradia CrystalCT scanner was employed, operating at 160 kV and 10 W with an HE18 source filter. A flat panel detector was used to image half of the fractured specimen, achieving a pixel size of approximately 3 μm. The data were analysed using DragonFly software, focusing on a region of interest (6.6 mm in diameter and 2.6 mm in height)

located 1 to 2 mm below the fracture surface.

2.4. In-situ neutron diffraction

The experimental setup of in-situ neutron diffraction is illustrated in Fig. 1a, and the applied load waveform is depicted in Fig. 1b. The experiment was conducted at the ENGIN-X beamline, a spallation neutron source allowing for simultaneous measurement of multiple grain orientations, namely, {111}, {200}, {220}, and {311}.

The test specimen was oriented at a 45° angle to the incident beam (Fig. 1a). Diffracted neutrons were collected by the axial and radial detectors placed at ± 90° to the incident beam, providing the lattice strain information along and perpendicular to the loading direction. To ensure good counting statistics, a 4 mm × 4 mm × 4 mm gauge volume was chosen, with a measurement time of 10 min per point. Specimen had a gauge diameter of 8 mm and length of 28 mm, Fig. S2b. Test temperature was maintained at 550 ± 3 ℃.

Due to potential misalignment issues with the in-situ rig during fully reversed fatigue test, continuous cycling was conducted at a strain amplitude of ± 0.3 %. Macroscopic strain data could not be measured using the extensometer, as it proved unreliable under cyclic loading. To address this, at the start of the test at 550 °C, a correlation coefficient was established between the rig's crosshead displacement and the strain derived from the stress-to-Young's modulus ratio. This enabled the test to run smoothly using displacement as the strain control mode. Further details are provided in the accompanying text of Fig. S5.

Fig. 1b illustrates the three primary load waveforms utilised for the in-situ neutron diffraction: (A) creep-fatigue S-F; (B) creep-fatigue F-S; (C) fast tension-fast compression. Note: Type C waveform was designed to accelerate the fatigue process. Within these waveforms, the fast strain rate was set at 1×10^{-3} /s and the slow strain rate at 3×10^{-5} /s. Additionally, continuous cycling was strain-controlled while creep was stress-controlled. Full details of each type of load waveform are outlined in Table S1, and the complete loading sequences are summarised in Table S2.

Neutron data collection was primarily conducted at the end of stress reversal and during the creep dwell, when the macroscopic strain reached peak tensile strain. Stress-free reference data were taken at the nominally unloaded state (i.e., 5 MPa in tension). The number of measurements was determined by the duration of the stress hold. Specifically, six measurements were conducted during a 60-minute peak dwell, whereas only one measurement was conducted during a 10-minute peak dwell.

Open Genie and GSAS data analysis suite was used to perform peak-fitting routines to determine the specific lattice spacings associated with the four grain families (refer to Fig. S6 for a typical diffraction pattern and indexed characteristic peaks). By knowing the stress-free lattice spacing as measured at the unloaded state, the lattice spacing measured under load was used to calculate the elastic lattice strain, $\varepsilon^{\mathrm{hkl}}$, for a family of grains which share the common {*hkl*} orientation:

$$\varepsilon^{hkl} = \frac{d^{hkl} - d_0^{hkl}}{d_0^{hkl}} \tag{1}$$

where d_0^{hkl} is the lattice spacing under a stress-free condition, and d^{hkl} is the lattice spacing measured when the specimen was under external load.

In addition to elastic anisotropy, when micro-yielding occurs, each grain family exhibits plastic anisotropy (Chen et al., 2014). Neutron diffraction only measures the elastic strain, and deviations from linearity in the lattice strain can be calculated for each grain family by subtracting the anticipated elastic lattice strain at the same stress level. The diffraction elastic constants (DECs), as reported in Wang et al. (2018) for 316 stainless steel at 550 ℃, are 190 GPa for {111}, 90 GPa for {200}, 165 GPa for {220}, and 125 GPa for {311}. These DECs were used to calculate the deviations from the linearity, to infer the effect of plastic deformation.

3. Crystal plasticity modelling

Crystal plasticity (CP) theory has been widely used to study the micro-mechanical behaviour of austenitic stainless steel under various conditions (e.g., tensile (Kocks and Mecking, 2003; Podesta et al., 2017), creep (Petkov et al., 2022) and fatigue (Lu et al., 2016; Pai et al., 2025)). The CP model employed in this study, which accounts for strain rate dependency, has been previously validated for polycrystalline materials such as zirconium (Liu et al., 2021, 2022) and titanium (Dunne et al., 2007; Zhang et al., 2016).

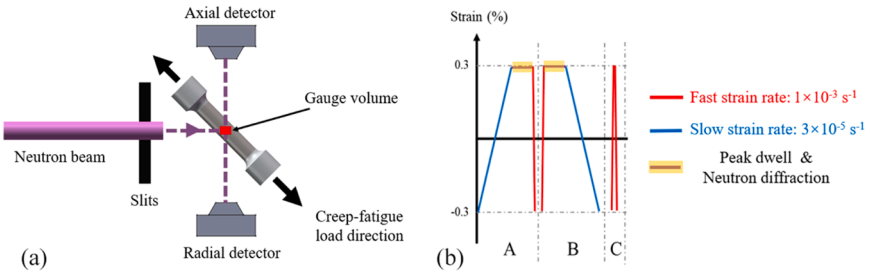

Fig. 1. (a) Arrangement of the specimen in the neutron diffraction ENGIN-X instrument; (b) illustration of asymmetric load waveform with the creep dwell. Type A waveform: creep-fatigue S-F; Type B: creep-fatigue F-S; Type C: fast tension-fast compression.

In this work, CP modelling was used to replicate laboratory testing conditions for S-F and F-S fatigue under the same strain amplitude and strain rates. The key features of the present CP modelling approach are summarised below.

The present implementation is based on the framework established by Dunne et al. (2007), with the primary modification being the statistically stored dislocations (SSDs) evolution to explicitly account for dynamic recovery processes during plastic deformation. The CP model incorporated 348 grains, over dimensions of $0.35 \times 0.35 \times 0.35\ mm^3$, proved sufficient to create a reliable digital twin of the physical grains. A comparison of the experimentally obtained pole figures with those predicted by the CP model is presented in Fig. S1b. Within the multiplicative elastic-plastic decomposition framework, the deformation gradient is split into elastic and plastic components (Roters et al., 2010; Zhang et al., 2016):

$$\boldsymbol{F} = \boldsymbol{F}^{e}\boldsymbol{F}^{P} \tag{2}$$

The evolution rate of the plastic deformation gradient ($\dot{\boldsymbol{F}}^{P}$) is determined by the plastic velocity gradient ($\boldsymbol{L}^{P}$), which is associated with plastic flow through active slip systems (Liu et al., 2022):

$$\dot{\boldsymbol{F}}^{P} = \boldsymbol{L}^{P}\boldsymbol{F}^{P} = \left(\sum_{s}\dot{\gamma}^{s}\boldsymbol{m}^{s}\otimes\boldsymbol{n}^{s}\right)\boldsymbol{F}^{P} \tag{3}$$

where $\dot{\gamma}^{s}$ is the shear strain rate of the slip system, with $\boldsymbol{m}^{s}$ and $\boldsymbol{n}^{s}$ representing the slip plane normal and directions, respectively.

The shear strain rate ($\dot{\gamma}^{s}$) for the s^{th} slip system, governed by thermally activated dislocation motion overcoming energy barriers, is expressed as (Cottrell and Dexter, 1954; Dunne et al., 2007):

$$\dot{\gamma}^{s} = \rho_{m}b^{s}v_{g} = \rho_{m}\omega(b^{s})^{2}exp\left(-\frac{\Delta F}{k\theta}\right)sinh\left(\frac{\Delta V}{k\theta}\left(\tau^{s}-\tau_{c}^{s}\right)\right) \tag{4}$$

where ρ_{m} is the mobile dislocation density, b^{s} is the magnitude of the Burgers vector for the slip system, and v_{g} is the average dislocation glide velocity. This accounts for both forward and backward dislocation jumps and when the resolved shear stress (τ^{s}) exceeds its critical value (τ_{c}^{s}), dislocation slip occurs. ω is the dislocation jump frequency, while the activation energy ΔF and activation volume ΔV are crucial parameters controlling the rate sensitivity of dislocation slip, and k represents the Boltzmann constant.

The magnitude of critical resolved shear stress (CRSS), symbolised as τ_{c}^{s}, depends on both the total SSDs and geometrically-necessary dislocations (GNDs) dislocation densities, following (Liu et al., 2022; Taylor, 1997):

$$\tau_{c}^{s} = \tau_{c,0}^{s} + Gb^{s}\sqrt{\rho_{SSD}+\rho_{GND}} \tag{5}$$

$$\rho_{SSD} = \sum_{s}\rho_{ssd}^{s} \tag{6}$$

$$\rho_{GND} = \sum_{s}\rho_{GND}^{s} \tag{7}$$

where $\tau_{c,0}^{s}$ represents the initial CRSS of the slip systems, and G denotes the shear modulus. ρ_{SSD} and ρ_{GND} represent the total SSDs and GNDs, respectively, while ρ_{ssd}^{s} and ρ_{GND}^{s} correspond to the dislocation densities per slip system. GNDs accommodate crystal lattice curvatures and thereby generate localised intragranular strain hardening. Its value can be calculated from the relationship between plastic deformation gradient curl and the Nye tensor (Arsenlis and Parks, 1999; Dunne et al., 2007):

$$\sum_{k=1}^{n}\left(\boldsymbol{b}^{s}\otimes\boldsymbol{S}^{s}\rho_{GND,s}^{s}+\boldsymbol{b}^{s}\otimes\boldsymbol{n}^{s}\rho_{GND,en}^{s}+\boldsymbol{b}^{s}\otimes\boldsymbol{m}^{s}\rho_{GND,et}^{s}\right) = curl\left(\boldsymbol{F}^{P}\right) \tag{8}$$

where $\rho_{GND,s}^{s}$, $\rho_{GND,en}^{s}$ and $\rho_{GND,et}^{s}$ represent the GND components, and $\boldsymbol{S}^{s}$, $\boldsymbol{m}^{s}$ and $\boldsymbol{n}^{s}$ represent the slip system orthogonal unit vectors, accounting for all edge and screw type dislocations within each slip system. The GND densities for all slip systems are computed using a constrained L2 minimisation scheme, which minimises the sum of squares of all GND components.

In contrast, the evolution rate of SSD densities is governed by the plastic strain rate and correlates with dislocation multiplication and dynamic recovery processes with respect to the current shear strain (Liu et al., 2022; Lu et al., 2019; Zepeda-Ruiz et al., 2017):

$$\dot{\rho}_{SSD} = k_{1}\dot{p} - k_{2}p = k_{1}\sqrt{\frac{2}{3}\boldsymbol{D}^{p}:\boldsymbol{D}^{p}} - k_{2}\int_{0}^{t}\dot{p}\ dt \tag{9}$$

where k_{1} and k_{2} are the proportionality constant representing the efficiency of dislocation generation and annihilation during plastic deformation. $\dot{p}$ and p represent the magnitude of the plastic strain rate and current shear strain, respectively, and $\boldsymbol{D}^{p}$ is the plastic strain rate tensor. In addition, the evolution law in Eq. (9) follows a non-linear dislocation hardening-recovery formulation rooted in Mecking and Kocks (1981) and implemented in similar form by Lu et al. (2019). The rate sensitivity arises from thermal activation mechanisms governed by ΔF and ΔV and widely validated in prior CP modelling studies (e.g. Benzing et al., 2019; Liu et al., 2022).Model parameters were initially calibrated using macro-mechanical experimental data from the first cycle and the saturation cycle, achieving stress amplitude predictions within a 20 % model-experimental error band. The key material parameters used in the CP modelling are

listed in Table 1, including elastic moduli, initial critical resolved shear stress, dislocation densities, and coefficients governing dislocation evolution and dynamic recovery processes.

4. Results

4.1. Macro-mechanical stress-strain response

Fig. 2 compares hysteresis curves obtained at the first and saturation cycles of fatigue and creep-fatigue tests, emphasising the effects of S-F and F-S load waveforms (represented by the black and red curves, respectively). The first cycle involves loading to a peak tensile strain of + 0.6 %, then reversing the direction to a peak compressive strain of −0.6 %, and finally changing the direction back to tension. The saturation cycle refers to the stable stage where the stress-strain response to cyclic loading becomes cycle-independent.

Overall, the difference between the S-F and F-S waveforms was more noticeable in the saturation cycle than the first cycle. This observation applies to both the fatigue and creep-fatigue tests. In the first cycle of fatigue tests (Fig. 2a), the hysteresis loops of the two waveforms were highly similar, with peak stress magnitudes of + 130 MPa and −148 MPa, respectively. As the tests progressed to the saturation cycle (Fig. 2b), the hysteresis loop for the F-S waveform shifted to the right compared to the S-F. Both the S-F and F-S waveforms exhibited higher stress amplitudes in their respective slow strain-rate loading phases. Additionally, a serrated stress pattern was observed during the slow strain-rate loading phase in both waveforms. At elevated temperatures and low strain rates, dynamic strain ageing (DSA) is a known mechanism that can induce instabilities in plastic flow, potentially leading to serrated features in the stress-strain response (Prasad Reddy et al., 2015a). The observed serrations may therefore be partially attributed to DSA. In addition, such features may also reflect a compromise in control performance between the fast- and slow-rate segments of the cycle, as the machine tuning parameters were optimised for the full waveform.

In the first cycle of creep-fatigue tests (Fig. 2c), the S-F and F-S waveforms exhibited similar changes during the tensile phase, but the F-S waveform consistently showed a higher stress level than the S-F waveform once the stress exceeded the yield strength of −70 MPa during the compression phase. In the saturation cycle (Fig. 2d), the differences between the S-F and F-S waveforms resembled those observed in the fatigue tests. However, compared to the fatigue tests, the overall stress amplitude was reduced. For example, for creep-fatigue S-F test shown in Fig. 2d, the stress values were 360 and −355 MPa at peak tensile and compressive strains during the saturation cycle. In comparison, for the fatigue S-F test shown in Fig. 2b, the corresponding stress values were 375 and −370 MPa.

Fig. 3 shows the peak tensile and compressive stress responses of the fatigue and creep-fatigue S-F and F-S tests, with the stress evolution plotted against the number of fatigue cycles. All four tests exhibited three characteristic stages of hardening, saturation, and softening, consistent with previous work on austenitic stainless steels (Srinivasan et al., 1999; Xie et al., 2019). For the present 316L stainless steel at 550 °C, the saturation stage was reached after 50 cycles. Comparing the fatigue S-F and F-S waveforms, the former entered the softening stage after 360 cycles, much earlier than the latter, which entered after 1200 cycles. In the creep-fatigue tests, both S-F and F-S waveforms exhibited an early onset of the softening stage, occurring after 160 cycles for the S-F and 300 cycles for the F-S waveform. This indicates that the introduction of creep dwells accelerates the softening process.

In comparison with the F-S waveform at the saturation stage, which had a tensile stress amplitude of 350 MPa, the S-F waveform displayed higher stress amplitude of 375 MPa for the fatigue test and 360 MPa for the creep-fatigue test, Fig. 3. In the compressive phase, the fatigue and creep-fatigue F-S tests exhibited higher stress amplitudes, with values of −390 MPa and −375 MPa, respectively. By comparison, the S-F tests at the saturation stage showed peak compressive stresses of approx. −370 MPa for the fatigue test and −355 MPa for creep-fatigue test. These distinct macro-mechanical stress-strain responses observed in the stress evolution curves of Fig. 3 are consistent with the single cycle observations shown in Fig. 2b and 2d.

In terms of the fatigue life, the fatigue F-S waveform had the life of 1500 cycles, while the S-F waveform had 444 cycles, representing a 70 % reduction. The introduction of tensile creep dwell led to a reduction in fatigue life. Specifically, incorporating a 1-hour creep dwell under the F-S waveform reduced the fatigue life by 77 %, from 1500 to 347 cycles. Under the S-F waveform, the 1-hour creep dwell resulted in a 54 % reduction in fatigue life, from 444 to 200 cycles. Although creep-fatigue tests generally result in a shorter fatigue life compared to pure fatigue tests, it is noteworthy that the overall duration of creep-fatigue tests exceeds that of fatigue tests due to the time consumption of the creep dwell (refer to Table S3).

Table 1
Modelling parameters for the material properties of 316L stainless steel at 550 °C.

Symbol	Description	Value
E_{11}	Elastic moduli (GPa)	140
G_{12}		76
ν_{12}	Poisson's ratio	0.31
$\tau_{c,0}$	CRSS of octahedral slip (MPa)	49
ρ_0	Initial dislocation density (μm^{-2})	0.1
k	Boltzmann constant ($J \bullet K^{-1}$)	1.3806×10^{-23}
ΔF	Activation energy (J)	2.77×10^{-19}
ΔV	Activation volume (μm)	$50\ b^3$
k_1	Dislocation hardening coefficient (μm^{-2})	160
k_2	Dislocation dynamic recovery coefficient ($\mu m^{-2} s^{-1}$)	8
ω	Dislocation jump frequency (s^{-1})	1×10^{11}

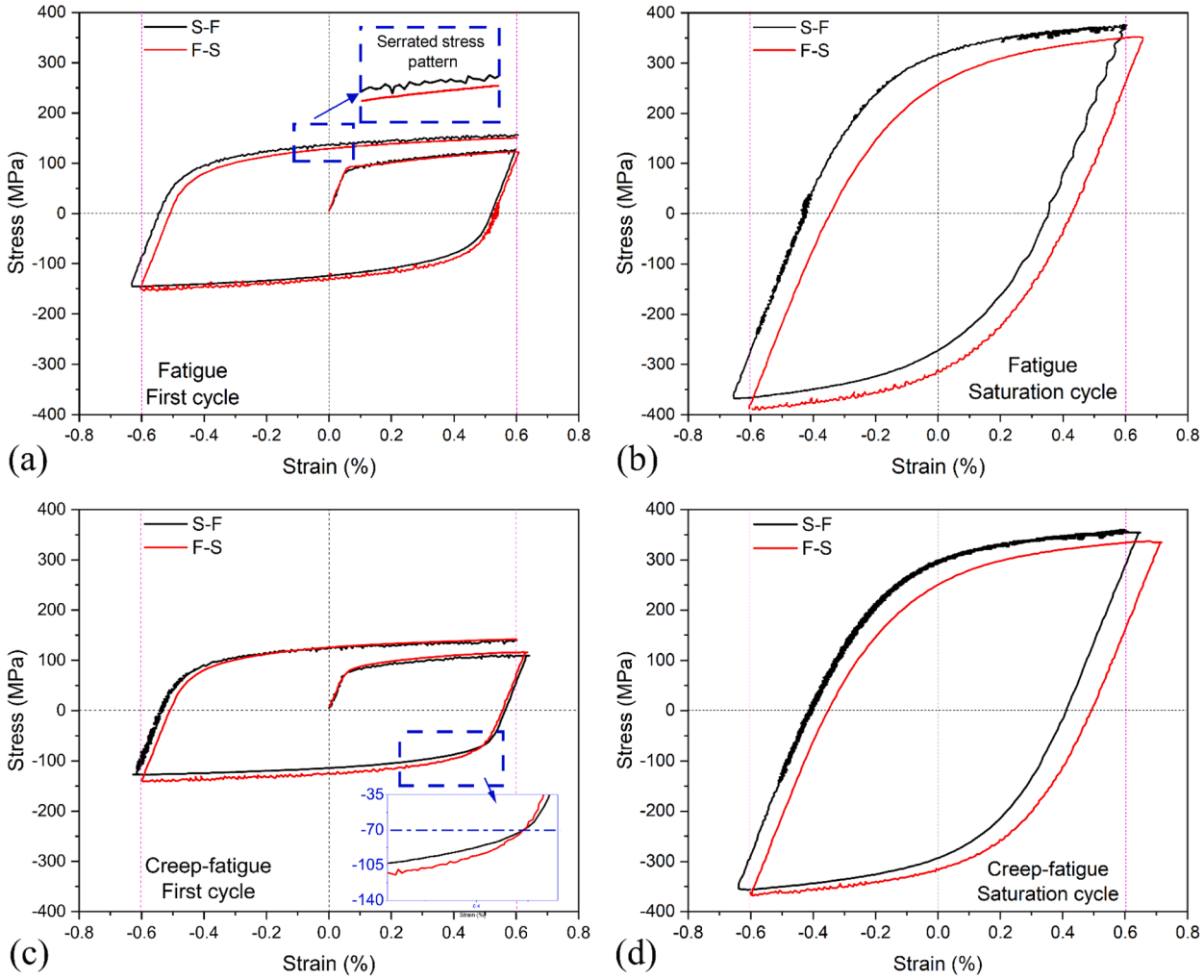

Fig. 2. Comparison of hysteresis loops for fatigue and creep-fatigue tests at the first and saturation cycles: (a) First and (b) saturation cycle for fatigue S-F and F-S tests; (c) first and (d) saturation cycle for creep-fatigue S-F and F-S tests.

Given the different fatigue lives across test conditions, normalising cyclic stress responses by fatigue life fraction facilitates direct comparison of the results (refer to Fig. S7). Compared to the F-S waveform, the transition from the saturation to softening stage tended to occur earlier in the S-F waveform. This observation suggests a more noticeable damage process occurring in the S-F waveform than in the F-S waveform.

4.2. Creep deformation

Creep deformation during the tensile dwell was measured under stress-controlled conditions, resulting in a forward creep response rather than stress relaxation. Due to the high data logging frequency (triggered by every 5.2 MPa or every 0.008 % strain change), the observed creep strain data during the peak stress hold per cycle exhibited a large fluctuation. Instead of employing subjective data smoothing, the Norton-Bailey model (Betten, 2008; May et al., 2013) and a power-law fit (represented by the blue and red curves, respectively) were used to illustrate the data trend in Fig. 4. Material parameters and statistical approach used to evaluate the error and uncertainty are detailed in Appendix A.

Fig. 4a to 4d compare the experimentally measured raw data with model predicted results in terms of creep strain accumulation during the tensile hold. Selected cycles from the S-F and F-S tests, representing the cyclic hardening and saturation stages, were used for this purpose. The measured creep strain was more consistent for the F-S test. Also, the data obtained during the saturation stage was more consistent than the hardening stage. The power-law fit exhibited a higher R-squared and similar RMSE values, although both models captured the overall trend of the measured data. As a result, the power-law fit was subsequently used for batch data fitting to all creep data.

Fig. 4e shows the evolution of the peak creep strain as a function of fatigue cycles. The peak creep strain slowly increased from 0.01

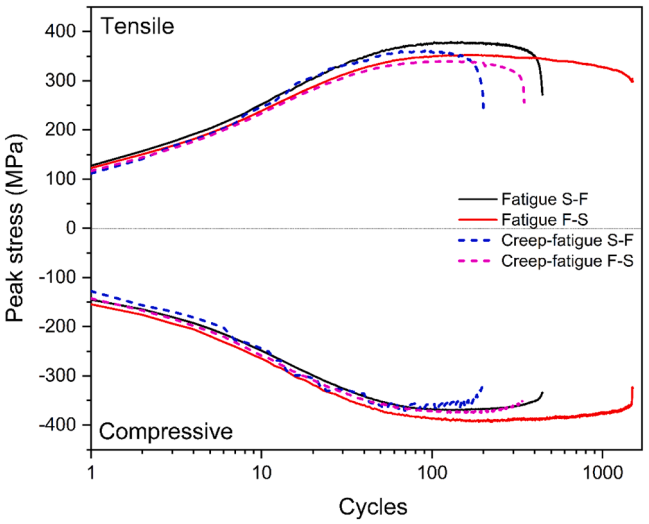

Fig. 3. Evolution of the peak tensile/compressive stress with respect to load cycles in different fatigue and creep-fatigue tests. Black and red solid lines represent fatigue S-F and F-S tests. Blue and purple dashed lines represent creep-fatigue S-F and F-S tests.

% to 0.04 % after 200 cycles under the F-S waveform, which is half of the increase observed with the S-F waveform, reaching 0.08 % at the same cycle count. For both waveforms, the peak creep strain increased rapidly during the cyclic hardening stage, then slowed down after approx. 50 cycles, corresponding to the start of the saturation stage. The observed peak creep strain jumps in Fig. 4e for the S-F test might be attributed to the unexpected temperature increase monitored at the middle of the S-F specimen centre after 100 cycles (Fig. S8). However, this anomaly does not affect the overall material behaviour, as confirmed by the similarity between the stress-strain curves of a typical outlier cycle and its adjacent cycles (Fig. S9).

Fig. 4f illustrates the evolution of creep strain over the creep dwell at selected cycles (5, 50,100, 200) for comparing the creep-fatigue S-F test with the F-S test. Both waveforms exhibited comparable creep behaviour in the initial cycle (5^{th} cycle). However, a more pronounced increase in creep rate was observed under the S-F waveform compared to the F-S waveform (50th cycle). The S-F waveform yielded a larger creep strain, reaching 0.05 % at the 100th cycle. In contrast, under the F-S waveform, creep strain increased much more slowly, reaching only 0.02 % at the 100th cycle. The S-F waveform consistently exhibited higher creep levels than the F-S waveform as the fatigue cycles progressed.

4.3. Failure modes and damage mechanisms

Fig. 5a and 5d show the overall fracture appearance of fatigue S-F and F-S specimens, where multiple crack initiation sites can be observed. In Fig. 5a, the blue area denotes a typical crack initiation region, the red area represents a typical transient fracture zone, and the intermediate area indicates the crack propagation region. In fatigue S-F test (Fig. 5b), the cracks initiated near the surface and propagated inward, leaving a distinct region of crack propagation, which appeared as fatigue striations. The transient fracture region (Fig. 5c) comprised a variety of sizes and shallow microvoids indicating the ductile fracture. Compared to the S-F test, the fatigue F-S specimen exhibited both surface and internal cracking (Fig. 5d and 5e), with fewer fatigue striations. Fig. 5f revealed a mixture of microvoids and cleavage fracture in the transient fracture zones.

In contrast to fatigue tests, both creep-fatigue S-F and F-S specimens predominantly exhibited intergranular fracture (Fig. 5g and 5j), and distinct fatigue striations were hardly observed. For these creep-fatigue specimens, due to the absence of clear crack initiation regions, the blue and red areas in Fig. 5g and 5j show representative fracture morphologies. In Fig. 5h, the creep-fatigue S-F specimen shows a significant dimpled rupture region at the centre, surrounded by numerous microvoids. Intergranular facets and cracks can be observed in Fig. 5i. In Fig. 5k and 5l, typical intergranular facets, cracks, and microvoids were also observed in the creep-fatigue F-S specimen. The introduction of creep clearly altered the overall fracture surface morphology, transitioning from fatigue-dominated to creep-dominated fracture features. While SEM fractography provided useful qualitative information about the fracture characteristics, it was not sufficient on its own to offer a quantitative assessment of the differences in failure modes between the S-F and F-S waveforms.

XCT was employed to provide quantitative data of internal defects by analysing the same sampling volume of 88 mm^3 (refer to Fig. S10) across all specimens. The XCT-identified defects for each sample condition were classified into near-spherical voids and irregular cracks based on their sphericity values (refer to Table S4 and associated text). Defect sizes ranged from 6.2 μm to 860 μm assessed using their volume-equivalent diameters. Given the large size range, defects were further classified into four groups: small (<20 μm), medium (20–120 μm), large (120–300 μm), and very large (>300 μm). The overall defect levels were identified as 3296 defects (0.04 vol. %) and 6439 defects (0.49 vol. %) for the fatigue S-F and F-S specimens, respectively. In comparison, creep-fatigue S-F and F-S specimens had a level of 5784 (0.87 vol. %) and 33,183 defects (0.04 vol. %), respectively. Fig. 6a shows a representative 3D visualisation of the XCT dataset collected from creep-fatigue S-F specimen, with different colours illustrating different defect size

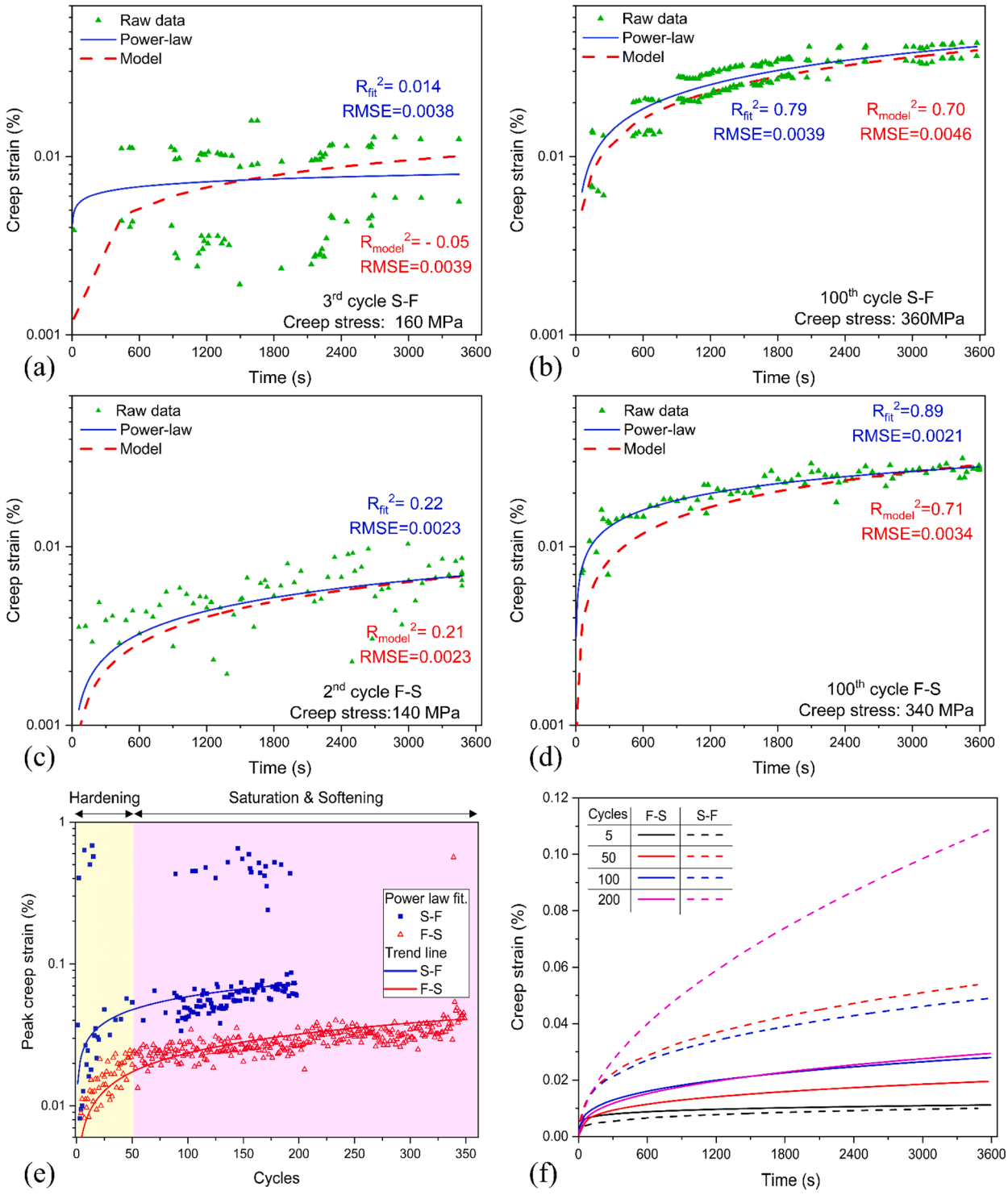

Fig. 4. (a)-(d) Comparison of experimental data, power-law fitted results, and model simulations for selected cycles in creep-fatigue tests: (a) 3rd cycle and (b) 100th cycle in the creep-fatigue S-F test; (c) 2nd cycle and (d) 100th cycle in the F-S test. Green symbols represent the original data, blue solid lines represent the power-law fitted, and red dashed lines represent the model predicted results. (e) Peak creep strain evolution and (f) accumulated creep strain for 5th, 50th, 100th, and 200th cycles.

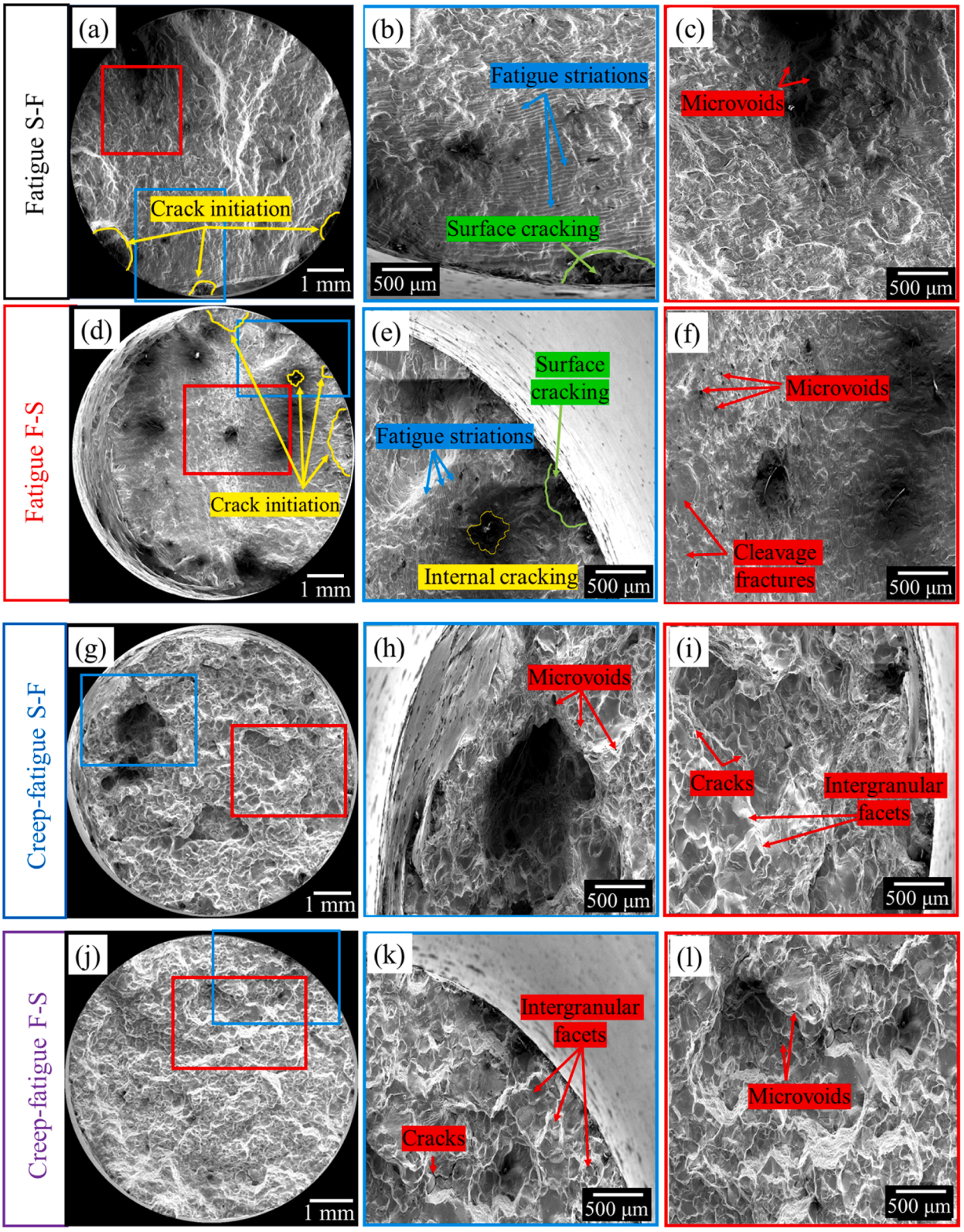

Fig. 5. Representative SEM fractography of fatigue and creep-fatigue specimens: (a-c) fatigue S-F; (d-f) fatigue F-S; (g-i) creep-fatigue S-F; and (j-l) creep-fatigue.

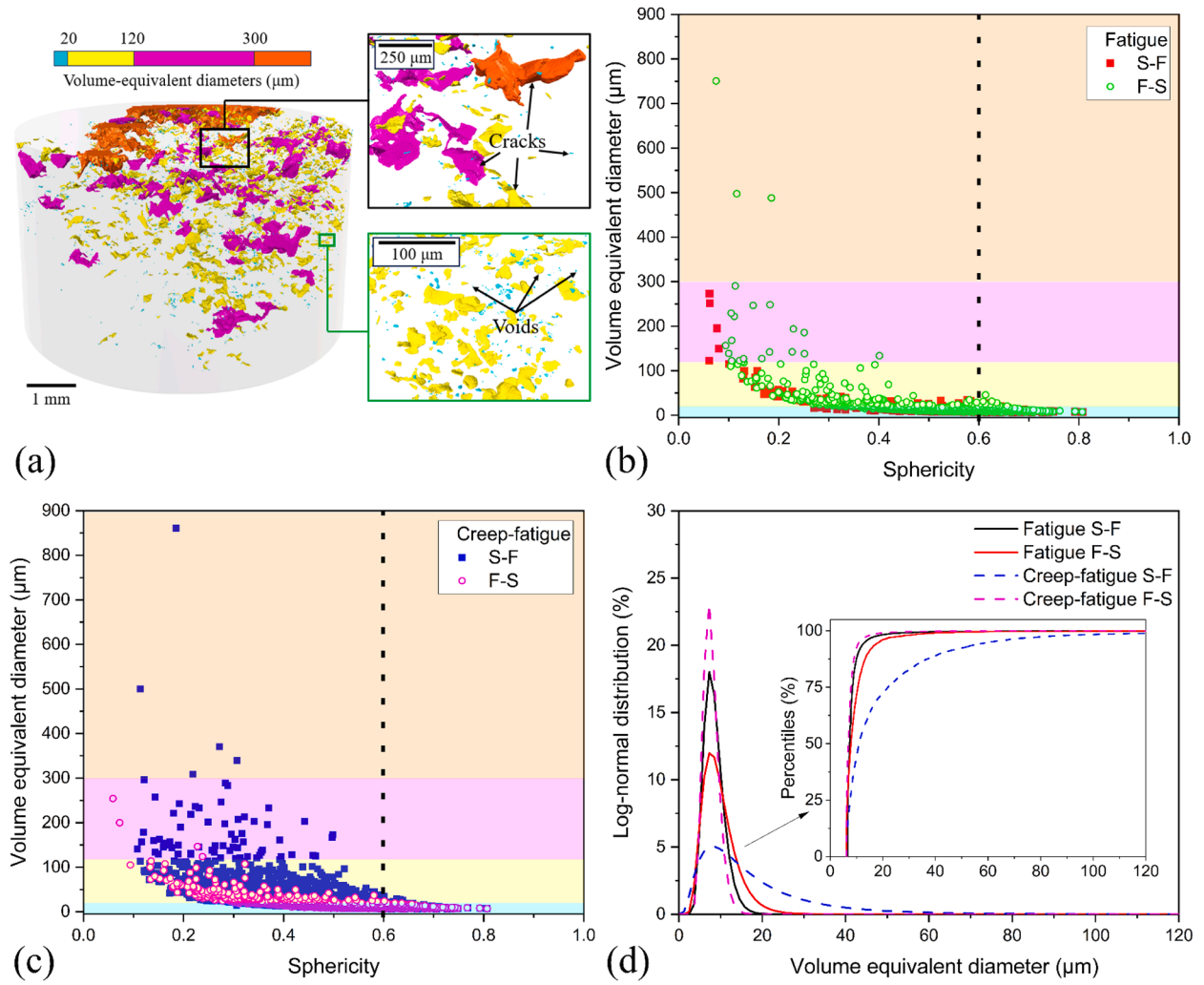

Fig. 6. XCT analyses of internal defects: (a) Representative 3D visualisation of the XCT dataset from creep-fatigue S-F specimen, with colours indicating different defect sizes. Distribution of defects in terms of volume-equivalent diameters and sphericity for (b) fatigued and (c) creep-fatigued specimens. Size classification: small (<20 μm), medium (20–120 μm), large (120–300 μm), and very large (>300 μm). (d) Comparison of the number-based size distribution plots.

groups. The magnified views show typical cracks in the black inset (top) and voids in the green inset (bottom).

Fig. 6b and 6c plot the distribution of defects in terms of their diameters and sphericity, for the fatigue and creep-fatigue specimens, respectively. The fatigue F-S specimen exhibited several defects exceeding 300 μm with sphericity of 0.1–0.2, indicating cracks. Compared to the S-F specimen, the F-S specimen had the higher number of defects in the size range of 120–300 μm, but their sphericity values were also lower than 0.6, indicating a less sharp micro-crack nature (refer to Table S4). Additionally, the vast majority of defects were in the small and medium size groups, accounting for 99.9 % and 99.4 % (number fraction) in the fatigue S-F and F-S specimens, respectively.

For the creep-fatigue specimens, the S-F waveform exhibited a considerably high number of defects (sphericity of smaller than 0.6) in the medium, large and very large size groups, when compared to the F-S counterpart. This suggests a higher likelihood for an intergranular failure mode. In addition, the vast majority of defects were in the small and medium size groups, accounting for 98.8 % and 99.9 % (number fraction) in the creep-fatigue S-F and F-S specimens, respectively. This observation is similar to the fatigue specimens.

Fig. 6d presents the log-normal number-based size distribution plots, together with their cumulative distribution plots, from which percentiles can be read directly from the vertical axis. This provides complementary information to that of volume-based one as already presented in Fig. 6b and 6c. Given that over 98 % of the defects have a diameter below 120 μm, the x-axis in Fig. 6d is set to a range of 0–120 μm. Four statistical parameters were derived from Fig. 6d, including location parameter, scale parameter, skewness, and kurtosis (refer to Table S5 for their meanings). The overall observation is that fatigue S-F, F-S, and creep-fatigue F-S specimens exhibited similar defect distributions, with the majority concentrated below 10 μm and median sizes of 7–9 μm based on the location

parameter. In contrast, the creep-fatigue S-F specimen had a larger median defect size of 14 μm. Moreover, the creep-fatigue S-F specimen had a higher proportion of defects in the size range of 10–40 μm, suggesting the presence of microcracks. This observation further corroborates its higher stress amplitude and shorter fatigue life. In terms of the detailed distribution characteristics, the fatigue S-F specimen had a low data dispersion and right-skewed distribution, while the fatigue F-S specimen exhibited greater data dispersion and more extreme values. The creep-fatigue S-F specimen had the highest median defect size and dispersion, approximating a normal distribution. In contrast, the creep-fatigue F-S specimen exhibited the lowest dispersion but a high right-skewness with numerous extreme values. In addition, systematic consistency checks were performed by analysing both halves of fractured fatigue S-F specimen to validate the representativeness of the post-fracture XCT analysis. The results demonstrate good agreement in defect volume fractions, size distributions, and spatial distributions between the two halves, confirming the reliability of the XCT methodology. Detailed comparative analysis is presented in the Supplementary Material (Fig. S11).

Given that the XCT scan region of interest has a height of approximately 2.6 mm (located 1 to 2 mm below the fracture surface), the defect volume distribution was analysed using 0.1 mm bin sizes. The results indicate that the majority of defects in all four specimens are concentrated at distances of 2–3 mm from the fracture surface. This spatial distribution is consistent across all test conditions, confirming that the defect analysis reflects bulk damage behaviour rather than fracture-surface effects. Detailed defect distribution analysis as a function of distance from the fracture surface is presented in the Supplementary Material (Fig. S12).

To summarise, both the SEM fractography and XCT defect analysis provide clear evidence of the significant impact of asymmetric load waveforms on fatigue and creep-fatigue damage processes.

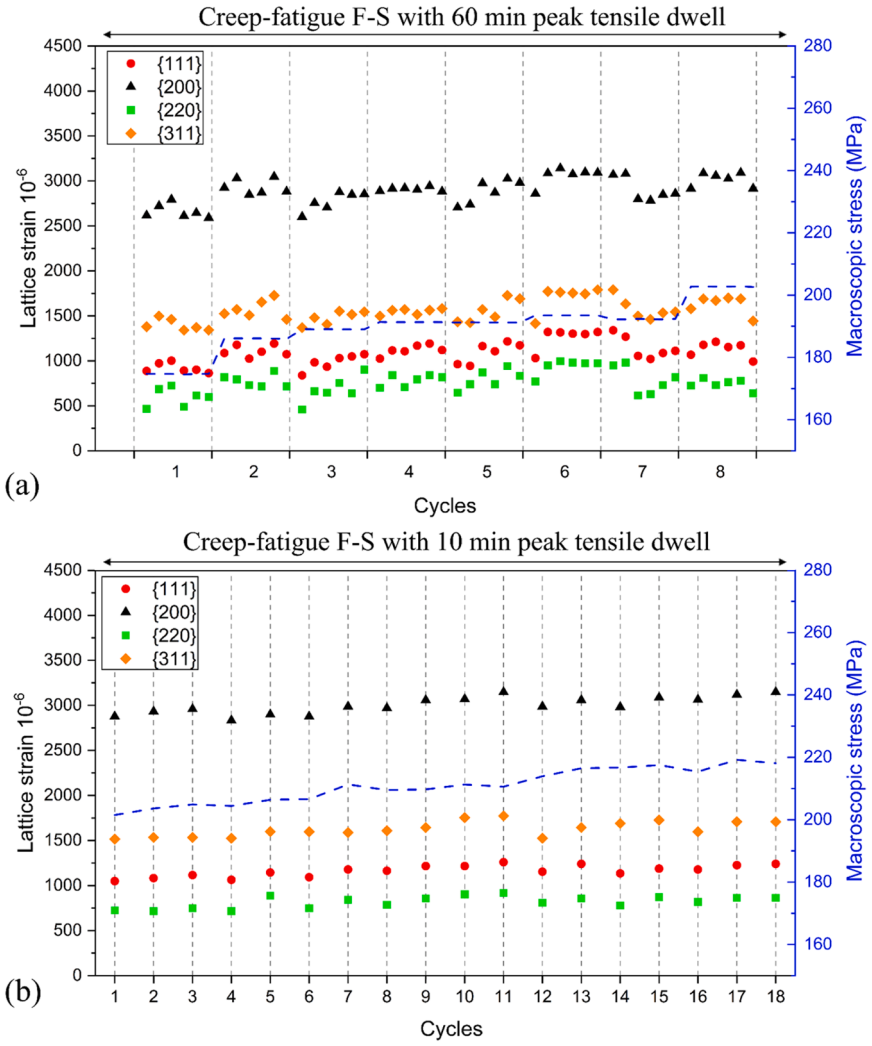

Fig. 7. Evolution of lattice strains from four major crystallographic orientations and the macroscopic stress: (a) module 1 (8 cycles of waveform B with a 60-minute tensile hold) and (b) module 2 (18 cycles of waveform B with a 10-minute tensile hold).

4.4. Micro-mechanical behaviour

In-situ neutron diffraction study involved four major modules, with each comprising one of the two waveforms (A: one S-F cycle; and B: one F-S cycle) or their combinations. Modules 1 and 2 were taken from the cyclic hardening stage, while modules 3 to 4 were taken from the saturation stage. Principles of designing the in-situ experiment are detailed in Appendix B.

Fig. 7 illustrates the evolution of elastic lattice strains, measured along the axial direction during the tensile dwell from the cyclic hardening stage. The load waveform closely resembled the creep-fatigue F-S test, with one cycle characterised by fast loading to the

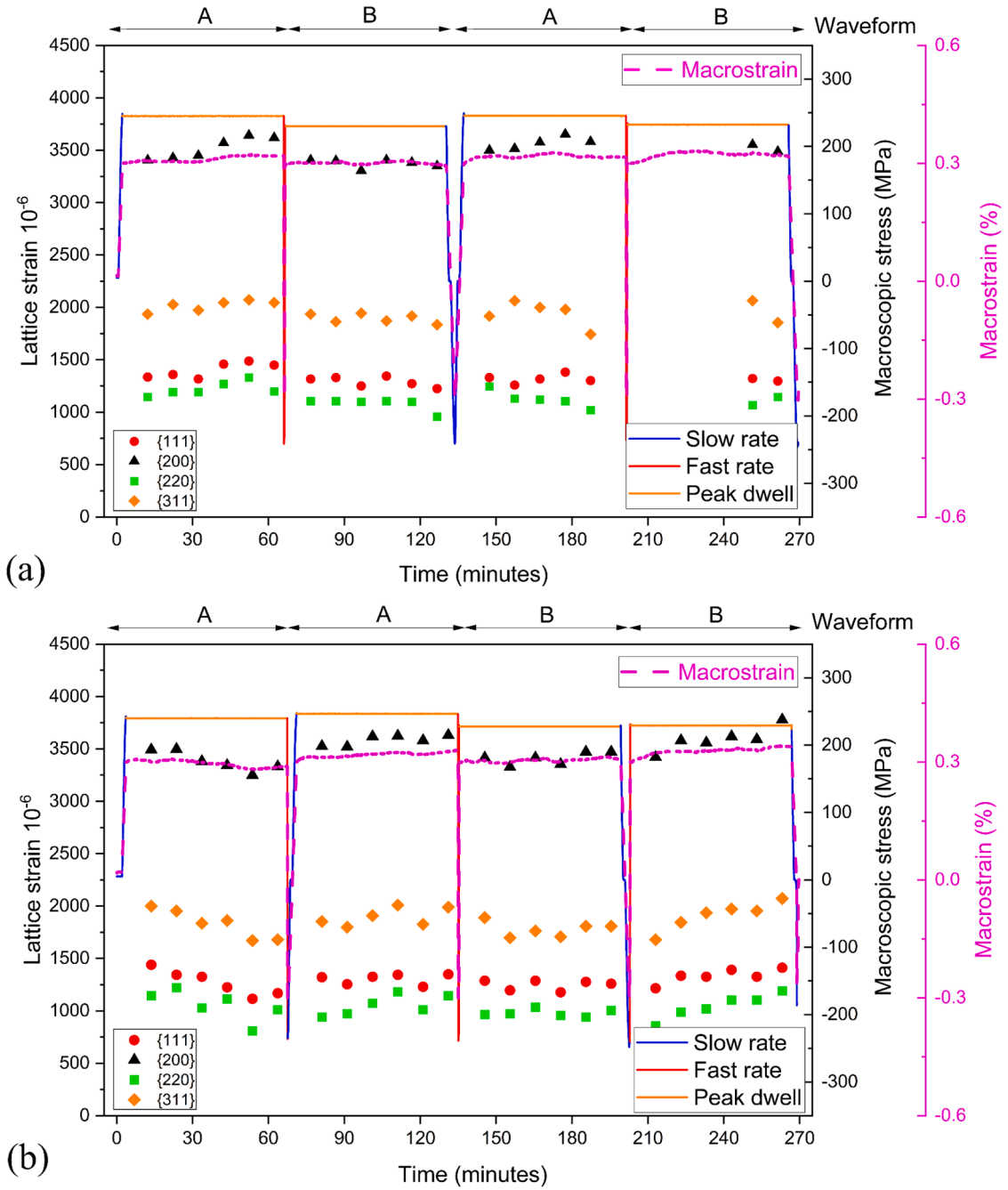

Fig. 8. Evolution of lattice strain, macroscopic stress and macrostrain in the cyclic saturation stage during asymmetric loading modules: (a) Module 3 (Waveform A-B-A-B) and (b) Module 4 (Waveform A-A-B-B). Waveform A and B represent one S-F cycle and F-S cycle. The solid and dashed lines represent macroscopic stress and macrostrain evolution, respectively, while symbols denote the measured lattice strains for {111}, {200},{220} and {311} grain families.

pre-defined tensile strain amplitude, holding at the corresponding peak stress (60-minute per cycle in Fig. 7a, whilst 10-minute per cycle in Fig. 7b), followed by slow reverse loading to the compressive strain amplitude. Upon the completion of initial loading to the macroscopic strain of + 0.3 %, the lattice strains of 900,2600, 470, and 1400 microstrains were developed for the {111}, {200}, {220}, and {311} grain families, respectively. These values are similar to the previous work (data comparison is presented in Fig. S13) (Mamun et al., 2019b; Wang et al., 2018).

During the 60-minute dwell, all grain families exhibited changes strongly correlated with macroscopic stress variations, Fig. 7a. In the first 60-minute dwell, all grain families showed an initial increase in lattice strain, which stabilised as the dwell period progressed. The increase in macroscopic stress consistently led to an increase in lattice strain across all grain families, and the trend of initial increase followed by stabilisation was observed in subsequent cycles. One exception to the general trend was observed when the macroscopic stress decreased, as seen in cycle 7 in Fig. 7a. In this case, the lattice strain initially decreased and then stabilised, further highlighting the link between macroscopic stress and lattice strain evolution. Over the 8 consecutive F-S cycles, the macroscopic stress rose from 180 MPa to 205 MPa, displaying a cyclic hardening phenomenon. Concurrently, the lattice strains of {200} and {220} grain families increased with the rising macroscopic stress, reaching values of 2900 and 720 microstrains, respectively. Given the observed changes in the grain families, with {220} exhibiting the lowest while {200} presenting the highest lattice strain, subsequent analysis will focus primarily on these two grain families.

Fig. 7b shows the lattice strain evolution during a 10-minute dwell introduced under 18 consecutive F-S waveform cycles. The lattice strains of {200} and {220} increased by 250 and 140 microstrains, respectively, as the macroscopic stress rose from 205 MPa to 220 MPa. Based on the elastic anisotropy of DECs, a macroscopic stress increase of 15 MPa would lead to a lattice strain increase of 167 microstrains for {200} grain family, while 91 microstrains for the {220} grain family. This suggests that the evolution pattern of the lattice strains closely followed the macroscopic stress variations.

Under longer creep durations (60 min, Fig. 7a), there was a noticeable increase in lattice strain followed by stabilisation. In contrast, under shorter creep durations (10 min, Fig. 7b), the lattice strain changes were more directly connected to increases in macroscopic stress. The measured data is highly reliable, as the value difference of lattice strain between the {111} and {222} grain families was within 100 microstrains (refer to Fig. S14).

Fig. 8a shows the lattice strain changes during the tensile dwells under a combination of A (creep-fatigue S-F) and B (creep-fatigue F-S) waveforms in the saturation stage. Upon completion of the slow-rate tension to a + 0.3 % strain amplitude, the {200} and {220} grain families exhibited lattice strains of 3400 and 1150 microstrains, respectively. During the 60-minute tensile dwell, the lattice strain increased and then stabilised at 3600 microstrains for the {200} and 1200 microstrains for the {220} grain families. After experiencing fast compression to − 0.3 % and fast tension to + 0.3 % strain amplitude, the initial lattice strains of {200} and {220} were 3400 and 1150 microstrains, respectively. Their reduced magnitudes can be attributed to the drop in macroscopic stress from 250 MPa to 230 MPa, causing an anticipated lattice strain contraction of 220 and 120 microstrains for the {200} and {220} grain families, respectively. During the 60-minute tensile dwell, no measurable change of the lattice strain was observed.

Following the waveform transition involving slow compression and slow tension, the initial lattice strains of {200} and {220} were 3400 and 1150 microstrains, despite the macroscopic stress increasing to 250 MPa. However, during the subsequent tensile dwell period, the phenomenon of lattice strain increasing and then stabilising reappeared. After the final transition through fast compression and fast tension, the macroscopic stress decreased again to 230 MPa. Unfortunately, the initial lattice strain values could not be captured due to the absence of the neutron beam. Nevertheless, the final values of the lattice strains for the {200} and {220} grain families after 60 min stabilised at 3500 and 1100 microstrains, respectively.

In Fig. 8b, following the initial slow tension, the lattice strains for the {200} and {220} grain families were 3500 microstrains and 1150 microstrains, respectively. However, the lattice strain first decreased and then increased to 3300 microstrains for {200} and 1000 microstrains for {220} during the 60-minute tensile dwell. After experiencing the transitions of fast compression and slow tension, the initial lattice strains of {200} and {220} changed to 3500 microstrains and 950 microstrains, respectively, with the macroscopic stress increasing from 240 MPa to 250 MPa. The lattice strains for {200} and {220} then increased to 3600 microstrains and 1150 microstrains within 30 min and remained unchanged for the rest of the dwell.

Following fast compression and fast tension to + 0.3 % strain amplitude, the macroscopic stress exhibited a similar downward trend as observed in Fig. 8a (from 250 MPa to 230 MPa). Correspondingly, the initial lattice strains of {200} and {220} decreased to 3400 microstrains and 950 microstrains, respectively. The subsequent 60-minute tensile dwell resulted in minimal lattice strain changes, with variations within 100 microstrains for all grain families. After the final transition through slow compression and fast tension, the macroscopic stress remained stable at 230 MPa. However, the lattice strain continued to increase during this period; after 60 min, the strains for {200} and {220} increased from 3400 microstrains and 900 microstrains to 3800 microstrains and 1200 microstrains, respectively.

Table 2
Calculated lattice strain deviation from linearity (in microstrains) from the measurements made after first loading to peak tensile strain over different modules.

Stress-strain stage	Module	{111}	{200}	{220}	{311}
Cyclic hardening	1	−32	675	−591	−18
	2	−11	637	−497	−95
Saturation	3	45	681	−340	−24
	4	176	826	−310	79

To summarise, the tensile peak dwell was influenced by the preceding load waveforms, with the slow-tension type tending to increase the macroscopic stress. The increased macroscopic stress caused the level of lattice strain to initially increase and then saturate. In contrast, macroscopic stress remained nearly constant following load cycles with fast tension before the dwell, with subsequent lattice strain showing minimal change. Additionally, the primary intergranular deformation incompatibility is most pronounced in the {200} and {220} grain families, as summarised in Table 2. Specifically, after initial loading to peak tensile strain, the {220} grain family exhibited a negative deviation from linearity, exceeding − 300 microstrains, and the {200} grain family showed a positive deviation greater than 600 microstrains (refer to Table S6 for the calculation method).

4.5. *Crystal plasticity model prediction*

CP modelling was employed to simulate up to 50 cycles of fatigue S-F and F-S tests, accurately capturing macroscopic behaviour and internal state evolution while maintaining computational efficiency. Fig. 9a compares experimentally measured peak tensile/compressive stresses with the CP model predictions, revealing good agreement, with stress amplitude deviations within 10 %. Specifically, the CP modelling captured the progressively higher peak stresses, namely, the cyclic hardening behaviour, for both S-F and F-S tests as the number of load cycles increased. The simulated macroscopic stress-strain responses for the individual cycles (e.g., first and saturation cycles as shown in Fig. S15) showed good agreement with experimental results.

Fig. 9b compares the accumulated dislocations from the CP model predictions for the fatigue S-F and F-S tests at both the first and saturation cycles, under the peak tensile strain of + 0.6 %. In the first cycle, S-F and F-S waveforms exhibited similar dislocation distributions with average dislocation densities (the sum of SSD and GND) of 54 μm^{-2} and 49 μm^{-2} respectively. However, in the saturation cycle, the dislocation density increased significantly under the S-F waveform, with average densities increasing to 186 μm^{-2}, compared to 147 μm^{-2} for the F-S waveform. According to Eq. (5), this higher dislocation density corresponds to an increased CRSS. Macroscopically, this reflects an increase in yield strength due to enhanced dislocation interactions, which would require higher stress levels to initiate plasticity. As a result, the experimentally observed higher stress amplitude for the S-F waveform, compared to the F-S waveform, can be attributed to the higher dislocation densities.

Regarding grain boundary responses in the CP modelling, the local fields at grain boundaries cannot be directly reflected in the experimentally measured lattice strain or creep strain, as both quantities represent averaged values over grain families or the entire polycrystal. Nevertheless, the simulated results show consistent trends with the experimental observations. Fig. 10 compares the lattice strain deviation from linearity of the {200} grain family and creep strain distribution for fatigue S-F and F-S conditions at peak tensile stress after 50 cycles. Visually, the S-F condition shows a broader distribution of high strain regions in both lattice and creep strain fields compared to the F-S condition. The quantitative results reveal that the lattice strain deviation from linearity under the S-F waveform reaches 823 microstrains, whereas the F-S condition shows only 612 microstrains, indicating higher grain-level deformation incompatibility accumulation. Additionally, the creep strain differences show S-F and F-S values of 0.038 % and 0.012 %, respectively, indicating that the S-F waveform induces more inelastic deformation and damage accumulation during tensile loading to peak stress at different rates. Note that the creep strain observed under fatigue loading arises from the accumulation of time-dependent inelastic strain during the slow-rate loading segments.

5. Discussion

5.1. *Effects of asymmetric load waveform*

The CP modelling suggests that the experimentally observed asymmetric stress response under S-F and F-S conditions arises from the rate-dependent evolution of dislocation structures. Fig. 11 shows the CP modelling simulated evolution of GND and SSD dislocation densities at three key loading points: (1) compressive yield point, (2) peak compressive strain, and (3) tensile yield point. During the

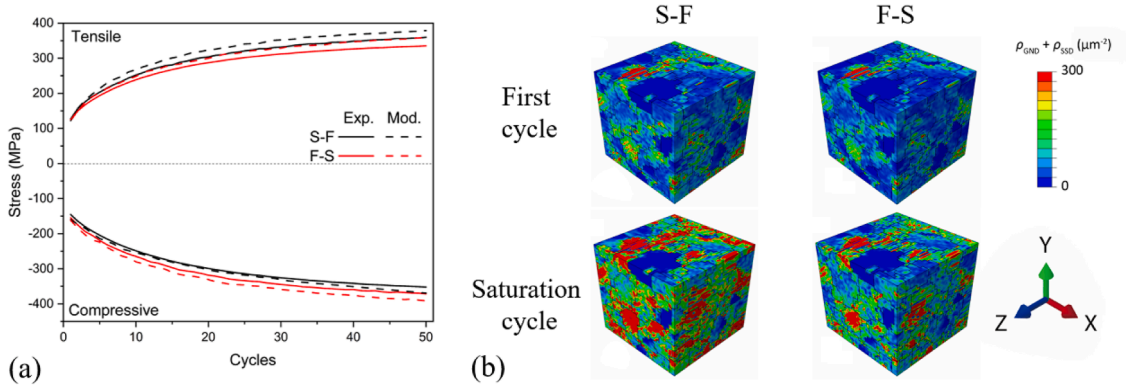

Fig. 9. Comparison of CP modelling with experimental data for fatigue S-F and F-S tests: (a) Peak tensile and compressive stresses from the first cycle to saturation cycle; (b) CP simulated dislocation distribution patterns at peak tensile strain for the first and saturation cycles.

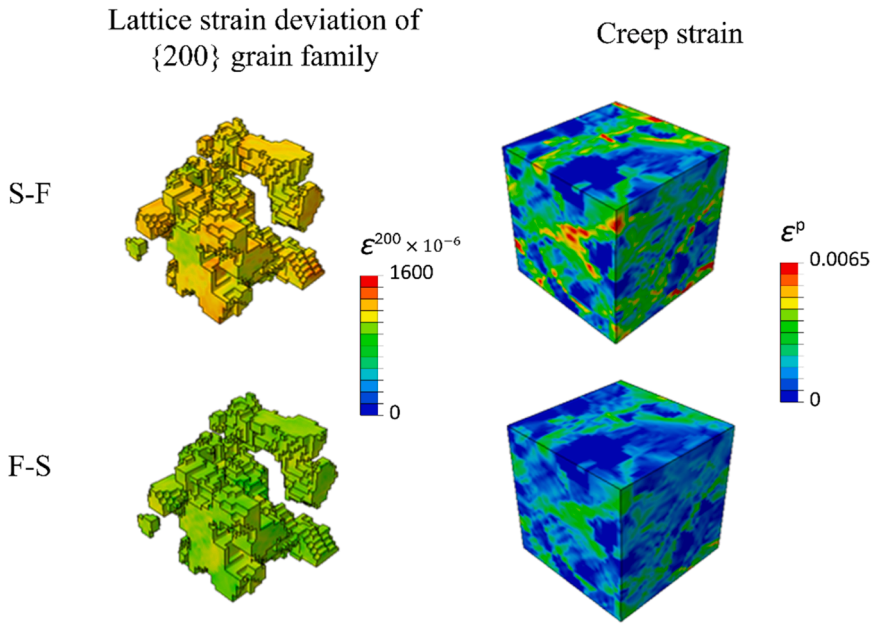

Fig. 10. CP modelling results at peak tensile stress after 50 cycles: lattice strain deviation from linearity for {200} grain family and creep strain distribution for S-F and F-S loading conditions.

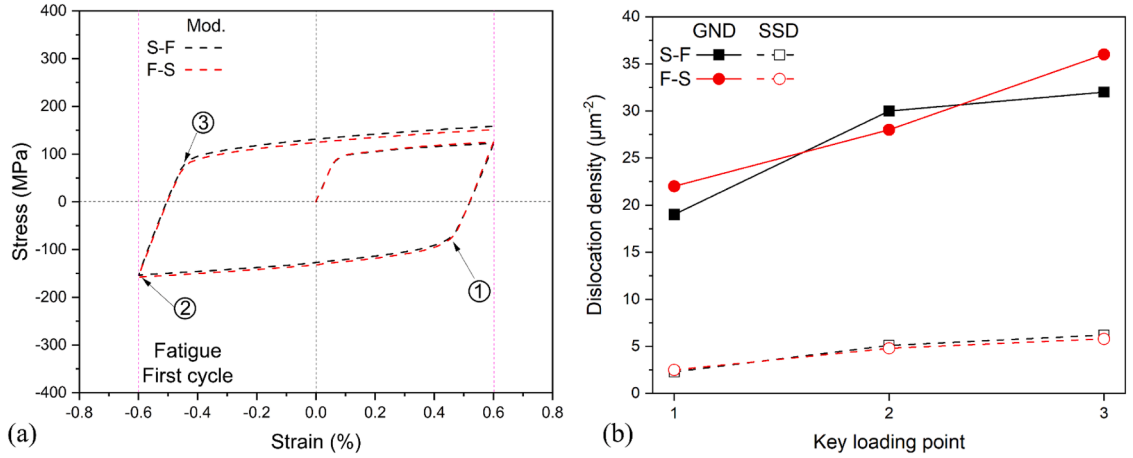

Fig. 11. CP modelling results for fatigue S-F and F-S tests: (a) stress-strain response during the first cycle showing three critical loading points: (1) compression yield point, (2) peak compressive strain, and (3) tension yield point; (b) respective GND and SSD density evolutions.

initial loading phase to peak tensile strain, GND contributions dominate the deformation process, accounting for over 80 % of the total dislocation density. The GND evolution, governed by the local plastic strain gradient curl, demonstrates strong rate sensitivity. During compression from point 1 to 2, the GND density in the S-F condition increases more significantly (from 19 μm^{-2} to 30 μm^{-2}, a 57 % increase) compared to the slow compression in F-S loading (from 22 μm^{-2} to 28 μm^{-2}, a 27 % increase). The higher GND accumulation rate in the compressive phase of S-F loading prevents lattice curvature and GND increase along the opposite direction. This explains why the F-S loading exhibits a greater increase in GND while loading reversal from point 2 to 3.

As cycling progresses, the SSD contribution, which depends heavily on plastic strain accumulation, gradually increases. At the saturation cycle under peak tensile strain, SSD densities reach 81 μm^{-2} and 55 μm^{-2} for the S-F and F-S conditions, comprising 37 % and 43 % of the total dislocation density, respectively. The higher dislocation densities (both GND and SSD) observed in S-F contribute to higher peak tensile stresses, leading to more pronounced differences between S-F and F-S responses at peak tensile strain (Fig. 9). This transition from GND-dominated to combined GND-SSD effects explains the distinct stress amplitudes observed during slow strain-rate loading phases through rate-dependent dislocation formation mechanisms.

In addition to influencing deformation behaviour, the asymmetric load waveform results in a longer fatigue life under F-S loading compared to its S-F counterpart, Fig. 3. This trend applies to both fatigue and creep-fatigue tests. At the saturation stage as shown in

Fig. 2b and 2d, the mean stress level for the F-S load waveform is −20 MPa, whereas for the S-F counterpart, it is + 3 MPa. It is generally expected that a compressive mean stress effectively slows fatigue crack growth. At room temperature, a previous study on 304 L stainless steel showed that a negative mean strain (−0.75 % and −0.25 %), accompanied by compressive mean stress (−7 and −5 MPa), can extend fatigue life by an order of magnitude compared to fully reversed fatigue testing (Colin et al., 2010). Conversely, a positive mean strain of 0.25 %, accompanied by a tensile mean stress of 15 MPa, resulted in a 35 % reduction in fatigue life relative to fully reversed fatigue testing. Therefore, the shorter fatigue life observed in the S-F load waveform can be attributed to the mean stress effect on fatigue crack propagation.

Furthermore, at 550 °C, as the strain rate decreases from the fast loading of 3×10^{-3} /s to the slow loading of 3×10^{-5} /s, the role of creep becomes increasingly significant. A strain rate of 10^{-4} /s is considered the critical threshold for the onset of creep process (Hales, 1980; Liang et al., 2023). Creep damage exhibits a positive correlation with stress level (Estrin and Mecking, 1984; Kachanov, 1999), where higher stresses accelerate the creep damage rate, leading to reduced lifespan (Ashby and Dyson, 1984). This stress-dependent damage accumulation mechanism explains the observed behaviour in the creep-fatigue S-F test, where the higher tensile stress amplitude (dashed blue curve in Fig. 3) enhances creep strain accumulation (Fig. 4e and 4f). Post-mortem examination of the creep-fatigue S-F specimen reveals a predominantly intergranular fracture mode (Fig. 5g) and the highest internal defect volume (0.867 vol %), with a greater proportion of medium-sized (10–40 μm) internal defects compared to other specimens. In summary, the combination of tensile mean stress and high tensile stress amplitude results in more pronounced creep deformation in the creep-fatigue S-F specimen, ultimately leading to the shortest fatigue life among the four test conditions.

The fatigue and creep-fatigue behaviour of 316 stainless steel has been extensively studied, enabling the establishment of master curves from the literature (Brinkman et al., 1972; Diercks and Raske, 1976; Prasad Reddy et al., 2015a, 2015b; Sauzay et al., 2004; Spindler, 2018; Xie et al., 2019; Yamaguchi and Kanazawa, 1980) to visualise the effect of waveform asymmetry on fatigue life at 550 °C. The multiple curves shown in Fig. 12 were fitted using the Manson-Coffin equation (Coffin Jr, 1954; Manson, 1953):

$$\frac{\Delta\varepsilon_t}{2} = \varepsilon_f'(2N)^c \tag{10}$$

where $\frac{\Delta\varepsilon_t}{2}$ is the total strain range, $2N$ is the number of reversals to failure, with ε_f' and C termed as fatigue ductility coefficient and fatigue ductility exponent, respectively. Two common trends are readily observed. First, under symmetric loading, a higher strain rate is associated with an extended fatigue life. Second, the reduction in fatigue life becomes more pronounced with increasing dwell time. Fatigue test employing the asymmetric F-S waveform (red upper triangle in Fig. 12) yields fatigue life comparable to that observed under symmetric loading with rapid strain rates. In contrast, the S-F waveform significantly reduces fatigue life (purple upper triangle in Fig. 12). Notably, the creep-fatigue S-F test results in a markedly shorter fatigue life, approximately 10 % less than that observed in fast symmetric loading with a 60-minute tensile dwell. From an experimental cost perspective, the S-F test reached sample failure in just 50 h, significantly shorter than the 684 h consumed for the creep-fatigue test under a symmetric load waveform. It should be noted that the focus of this study is not on the statistical evaluation of fatigue life, but rather on establishing mechanistic understanding of creep-fatigue interaction under asymmetric load conditions. Additional tests to support statistical reproducibility are planned as part of future work.

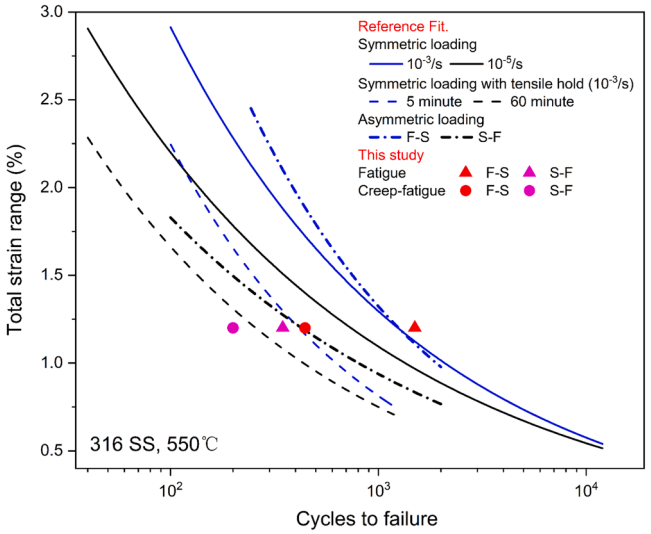

Fig. 12. Effect of fatigue loading waveform on the number of cycles to failure for 316 stainless steels (SS) at 550 °C under various conditions. Results from this study are compared with literature data (Brinkman et al., 1972; Diercks and Raske, 1976; Prasad Reddy et al., 2015a, 2015b; Sauzay et al., 2004; Spindler, 2018; Xie et al., 2019; Yamaguchi and Kanazawa, 1980). Refer to Table S7 and its associated text for further details.

5.2. Correlation between macroscopic and micro-mechanical behaviour

This study highlights a strong correlation between macroscopic and micro-mechanical behaviour. Specifically, the neutron diffraction results in Fig. 7 and Fig. 8 clearly show that the {200} grain family undergoes the most significant grain-level deformation during tensile holds. This behaviour is characterised by an initial increase in lattice strain, followed by saturation, which appears to correlate positively with the higher macroscopic stress induced by slow-tension loading.

The relationship between lattice strain and macroscopic behaviour is typically linear during the elastic stage but becomes nonlinear in the plastic regime. From a micro-mechanical modelling perspective, the {200} grain family is expected to show significant nonlinearity and residual strain accumulation beyond the elastic regime during uniaxial tension (Hu et al., 2015; Hu and Cocks, 2016). This nonlinearity reflects intergranular stress redistribution and the activation of intragranular slip systems (Clausen et al., 1999, 1998) and its presence is indicative of the onset of micro-yielding (Petkov et al., 2019).

Following high-temperature creep, the {200} grain family exhibited tensile (positive) lattice strain deviations from linearity and misfit stress (Chen et al., 2014, 2015b). In addition, the measured lattice strain changes in the {200} grain family during stress reversal and reloading processes were believed to play a crucial role in adjusting internal stress and ensuring deformation compatibility, particularly in relation to primary creep regeneration (Li et al., 2021; Mamun et al., 2020). Furthermore, Wang et al. (2013) compared lattice strain changes between the strain- and stress-control modes over 900 s. Under the strain hold mode, both lattice strain and macroscopic stress decreased by 10 % rapidly before stabilising, whereas under the stress hold mode, lattice strain remained nearly constant, despite a significant increase in creep strain, reaching up to 1.5 %. Under cyclic loading, the lattice strain in the {200} grain family gradually increased with the number of cycles, rising from approximately 3000 microstrains at the 8^{th} cycle to 3600 microstrains at failure (around 700 cycles), suggesting evolving intergranular stresses throughout the fatigue process (Li et al., 2019).

The present neutron diffraction measurements represent the first attempt to elucidate the effect of stress hold on lattice strain evolution under an asymmetric fatigue waveform. For this purpose, lattice strain changes in the {200} grain family were extracted over a 60-minute period during the cyclic saturation stage under creep-fatigue S-F and F-S loading conditions, shown in Fig. 13 using black and red, respectively. Here, the stress hold-induced lattice strain is defined as the change from the initial lattice strain measured at the start of each stress hold. In addition, literature data on 316H stainless steel at 650 °C under stress-controlled creep-fatigue conditions (Li et al., 2021; Mamun et al., 2020) were considered for comparison. One study (Li et al., 2021) did not specify the loading rate, while the other (Mamun et al., 2020) used 5 MPa/s; both classified as fast-rate loading. To ensure a like-for-like comparison, the analysis was limited to the initial 60 min of each chosen cycle. The trend curves in Fig. 13 were fitted using second-order regression.

A direct comparison of stress hold-induced lattice strain in the {200} grain family between the creep-fatigue S-F and F-S tests reveals distinct evolution patterns. Under F-S loading, the lattice strain fluctuates within 100 microstrains, whereas under S-F loading, a gradual increase is observed, reaching approximately 150 microstrains after 60 min. This increasing trend is also evident in the 316H stainless steel datasets, where a 155 MPa tensile stress hold resulted in a change of 150 microstrains, while the 140 MPa tensile stress hold led to approximately 300 microstrains. These observations indicate that tensile stress hold promotes higher grain-level deformation incompatibility.

It is well recognised that GNDs play a crucial role in accommodating deformation compatibility between differently oriented grains in polycrystalline materials, serving as an indicator of intergranular damage (Ashby, 1970; Muránsky et al., 2019). Our CP modelling results reveal higher GND densities at peak tensile strain under S-F loading in both the first and saturation cycles, indicating greater grain-level deformation incompatibility compared to the F-S counterpart.

In addition, the dislocation density differences observed in the modelling results stem from the rate-dependent evolution of both

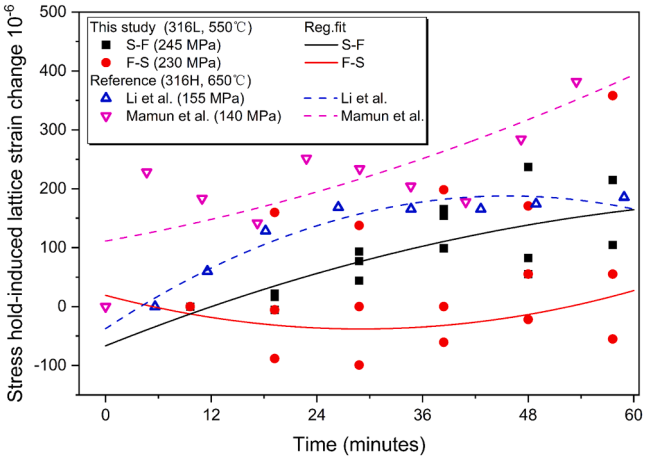

Fig. 13. Effect of stress hold on lattice strain evolution in the {200} grain family, shown as the change in measured lattice strain relative to its initial value at the start of each stress hold. This change is interpreted as stress hold-induced lattice strain for comparative analysis. The curves were derived from second-order regression fits applied to data obtained from the present work and literature data (Li et al., 2021; Mamun et al., 2020).

GND and SSD densities during asymmetric loading, where GND density is governed by plastic strain gradient curl while SSD density evolution depends on the balance between dislocation multiplication and dynamic recovery. The "curl of the plastic strain" is a mathematical concept in strain-gradient plasticity theories (Liu et al., 2022), where it represents a Burgers vector tensor that quantifies plastic incompatibility within a material. The different strain rate sequences in S-F vs F-S loading result in different plastic strain accumulation histories, where the S-F condition experiences more severe dislocation multiplication during the slow tensile phase with insufficient time for dynamic recovery. The combination of these rate-dependent mechanisms results in higher total dislocation densities in S-F conditions, which directly translates to higher CRSS values through the Taylor hardening relationship (Taylor, 1997) and consequently higher macroscopic stress amplitudes.

5.3. Creep-fatigue damage calculation

To quantify the relative contributions of creep and fatigue damage under asymmetric loading condition, a time-dependent damage model was employed. This model follows the linear damage accumulation rule, which assumes that total damage results from the independent accumulation of fatigue and creep damage components (Taira, 1962). The fatigue damage per cycle, d_f, is calculated as follows (Skelton and Gandy, 2008; Taira, 1962):

$$d_f = \frac{1}{N_{fi}} \tag{11}$$

where N_{fi} is the number of cycles to failure under fatigue loading at a fixed strain range, experimentally determined to be 444 and 1500 for the fatigue tests using S-F and F-S waveforms, respectively. Creep damage per cycle, estimated using the time fraction rule, is calculated as (Spindler, 2005, 2018):

$$d_c^{TF} = \int_0^{t_h} \frac{d_t}{t_f(\sigma)} \tag{12}$$

where t_h is the dwell time and t_f is the creep rupture time at a given stress level. The function $t_f(\sigma)$ was derived from the creep rupture data of 316L stainless steel (Spindler, 2018) and fitted using a logarithmic relationship:

$$\lg(t_f) = \beta_0 + \beta_1 . \lg(\sigma) \tag{13}$$

where the fitting coefficients β_0 and β_1 are 25.23 and −8.826, respectively.

Alternatively, creep damage can be quantified using the ductility exhaustion model (Takahashi, 2008), which is particularly effective for evaluating creep-dominated damage mechanisms in austenitic steels under complex loading conditions (Oh et al., 2011; Wen et al., 2016). According to this model, creep damage per cycle is given by Spindler and Payten (2011), Spindler (2004):

$$d_c^{DE} = \int_0^t \frac{\dot{\bar{\varepsilon}}_c}{\bar{\varepsilon}_f(\dot{\bar{\varepsilon}}_c)} dt \tag{14}$$

where $\dot{\bar{\varepsilon}}_c$ is the instantaneous von Mises equivalent creep strain rate and $\bar{\varepsilon}_f(\dot{\bar{\varepsilon}}_c)$ is the uniaxial creep strain at failure. The stress amplitudes during the cyclic saturation stage of the creep-fatigue tests are 360 MPa and 340 MPa for the S-F and F-S waveforms, respectively. A uniaxial creep strain to failure value of 0.15, derived from reference creep tests conducted at 333 MPa and 550 °C (Spindler, 2018), was adopted to ensure comparability with the stress level in the current study. The $\dot{\bar{\varepsilon}}_c$ value was determined via power-law fitting of the measured creep strain per cycle, normalised to a 1-hour dwell time.

The total damage was computed using the linear damage summation rule (Ainsworth, 2006):

$$D = D_f + D_c = \sum_j n_j d_{fj} + \sum_j n_j d_{cj} \tag{15}$$

in which D, D_f and D_c are the total, creep and fatigue damage respectively; n_j is the number of cycles; d_{fj} and d_{cj} are the fatigue and creep damage components per cycle. Considering the different methodologies for creep damage calculation, total damage was categorized into time fraction and ductility exhaustion approaches for comparative analysis.

Fig. 14a shows the fatigue, creep, and total damage at failure for the creep-fatigue S-F and F-S tests. The failure cycles for the creep-fatigue S-F and F-S tests are 200 and 347, respectively. In the S-F test, fatigue damage at failure was 0.45. The time fraction method led to a non-conservative prediction, estimating creep damage as 0.28 and total damage as 0.73. Conversely, the ductility exhaustion model provided a more conservative prediction, with creep and total damage at failure reaching 0.73 and 1.18, respectively. Similarly, the fatigue damage at failure was 0.23 for the F-S test, with creep damage predictions of 0.32 and 0.66 based on the time fraction and the ductility exhaustion approaches, resulting in total damages of 0.55 and 0.89. The evolution of fatigue, creep, and total damage with respect to the load cycles for the creep-fatigue S-F and F-S tests can be found in Fig. S16.

Fig. 14b shows the creep-fatigue damage interaction diagram. Under asymmetric loading waveforms, the time fraction method generally underestimates total damage, rendering it non-conservative for damage assessment. In contrast, the ductility exhaustion model provides predictions that align more closely with experimental observations. Both approaches indicate that the S-F waveform

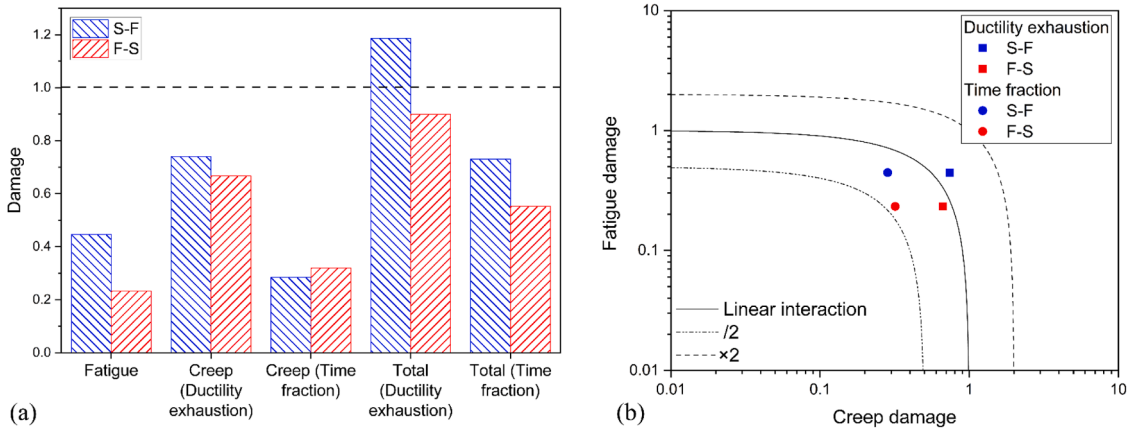

Fig. 14. (a) Comparison of fatigue, creep, and total damage at failure for creep-fatigue S-F and F-S tests, calculated using the time fraction and ductility exhaustion methods. (b) Creep-fatigue damage interaction diagrams for creep-fatigue S-F and F-S tests.

induces greater creep damage compared to the F-S waveform. According to the ductility exhaustion model, creep damage predominates in both creep-fatigue S-F and F-S scenarios, which correlates with post-mortem fracture analyses. The absence of fatigue striations and the prevalence of intergranular features in the creep-fatigue failed specimens (Fig. 5) further confirm the creep-dominated failure mechanism.

6. Conclusion

This study investigates the creep-fatigue interaction in Type 316L stainless steel under an uncommon asymmetric load waveform from both macro- and micro-mechanical perspectives. The key conclusions are as follows:

1. The slow-rate loading phase induces higher stress amplitude, leading the S-F waveform to generate greater tensile stress amplitude than its F-S counterpart in both fatigue and creep-fatigue tests. Consequently, the peak creep strain during the tensile dwell in the creep-fatigue S-F waveform is twice that of the F-S condition.
2. Neutron diffraction measurements reveal that the greater lattice strain accumulation during the tensile dwell is driven by the higher stress amplitude induced by the slow-rate loading phase, with the lattice strains typically showing an initial increase followed by stabilisation.
3. Crystal plasticity modelling interprets that the higher stress amplitude observed in the slow-rate tensile loading of S-F waveform originates from the faster dislocation accumulation. In the saturation cycle, dislocation densities reach 186 μm^{-2} and 147 μm^{-2} for the S-F and F-S waveforms, respectively, compared to 54 μm^{-2} and 49 μm^{-2} in the first cycle.
4. Both creep-fatigue S-F and F-S specimens exhibit a predominant intergranular fracture, indicating a clear transition from transgranular fatigue to creep-dominated damage. Additionally, the creep-fatigue S-F specimen shows the highest level of internal defects and a higher prevalence of microcracks. Creep-fatigue life assessment based on the time fraction method generally underestimates damage, whereas the ductility exhaustion method yields predictions that more closely match experimental observations.

CRediT authorship contribution statement

Fan Wu: Writing – original draft, Visualization, Investigation, Formal analysis. **Yang Liu:** Visualization, Software, Resources, Methodology. **Huayue Zhang:** Writing – review & editing, Investigation. **Christos Skamniotis:** Writing – review & editing, Investigation. **Umer Masood Chaudry:** Investigation, Formal analysis. **Gareth Douglas:** Writing – review & editing, Resources, Investigation. **Joe Kelleher:** Investigation. **Andrew Wisbey:** Resources. **Mike Spindler:** Resources. **Marc Chevalier:** Resources. **Bo Chen:** Writing – review & editing, Supervision, Methodology, Investigation, Funding acquisition, Conceptualization.

Declaration of competing interest

The authors declare that they have no known competing financial interests or personal relationships that could have appeared to influence the work reported in this paper.

Acknowledgements

This work received financial support from the UK's Engineering and Physical Sciences Research Council (EPSRC), Early Career

Fellowship Scheme (EP/R043973/1) awarded to BC. We thank the ISIS Neutron and Muon Source in the UK for awarding ENGIN-X beamtime RB2010070; and the creep-fatigue testing rig access at UK's High Temperature Facility (HTF) Alliance. We acknowledge the use of facilities within the University of Leicester (UoL) Advanced Microscopy Facility and for the access to the Hercules, funded by the EPSRC Strategic Equipment Scheme (EP/X014614/1) – Correlative Analysis of Crystals in 3D. FW and BC acknowledge Dr Yiqiang Wang, UKAEA, and Mr An Chen, University of Bristol, made contributions to the neutron diffraction measurements, and Mr Antony Xavier Ramesh, UoL, for assisting with the XCT characterisations.

Supplementary materials

Supplementary material associated with this article can be found, in the online version, at doi:10.1016/j.jmps.2025.106353.

Appendix A. Norton-Bailey model and a Power-law fit to creep dwell data

The Norton-Bailey model which includes both the primary and secondary creep regimes depicts the creep strain, ε_{cr}:

$$\varepsilon_{cr} = A\sigma^n t^m \tag{A1}$$

where *A*, *n*, and *m* are temperature-dependent material constants, and their values are shown in Table A1. Note that the stress magnitude was updated for each cycle to reflect the actual peak tensile stress measured at the start of the creep dwell.

Table A1
Parameters used for simulating the creep evolution in creep-fatigue S-F and F-S tests.

Test	A ($MPa^{-n}hr^{-m-1}$ %)	N	M
F-S	2.559×10^{-6}	1.6	0.494
S-F	2.955×10^{-6}	1.6	0.385

The power-law fit was performed using the MATLAB fitting routine with the equation:

$$\varepsilon_{cr} = Bt^k \tag{A2}$$

where B and k are constants. An iterative process was used to optimise the parameters of the power-law fit, ensuring convergence to the best-fit value. During each iteration, the fitting algorithm adjusted the values of B and k to minimise the difference between the observed creep strain and the fitted results, leveraging a nonlinear least squares methodology. The iteration process terminated once the parameter values fell below the threshold of 1×10^{-8}.

The root mean square error (RMSE) and R-squared metrics were used to evaluate the error and uncertainty of the model prediction. These metrics provided quantitative assessments of the model's ability to capture the variability in the experimental data:

$$RSME = \sqrt{\sum_i^n \frac{(y_i - \widehat{y}_i)^2}{n}} \text{ (A3) } R^2 = 1 - \frac{\sum_i (y_i - \widehat{y}_i)^2}{\sum_i (y_i - \overline{y})^2} \tag{A4}$$

where y_i, $\widehat{y}_i$, and $\overline{y}$ are the experimentally measured raw data, model predicted results, and the average of the raw data, respectively.

Appendix B. Principles of designing in-situ creep-fatigue study

Although it is practically impossible to conduct a creep-fatigue test at a beamline due to instrument and time limitations, it is important to ensure that the material behaviour observed from the two tests is comparable. Fig. B1 compares the peak tensile and compressive stress responses from the in-situ neutron diffraction study with those of the fatigue F-S test conducted in the laboratory. The observed stress-amplitude difference of 110 MPa at the saturation stage between the two aligns perfectly with expectations. In the work by (Sauzay et al., 2004) on 316L(N) stainless steel at 550 °C, the stress amplitude at the saturation stage under a ± 0.3 % strain amplitude was found to be 235 MPa, while it was 345 MPa under a ± 0.6 % strain amplitude, resulting in a stress difference of 110 MPa. This good consistency demonstrates that the micro-mechanical behaviour studied via the in-situ neutron diffraction measurements can provide a reliable basis for interpreting the laboratory tests, despite the strain-amplitude difference.

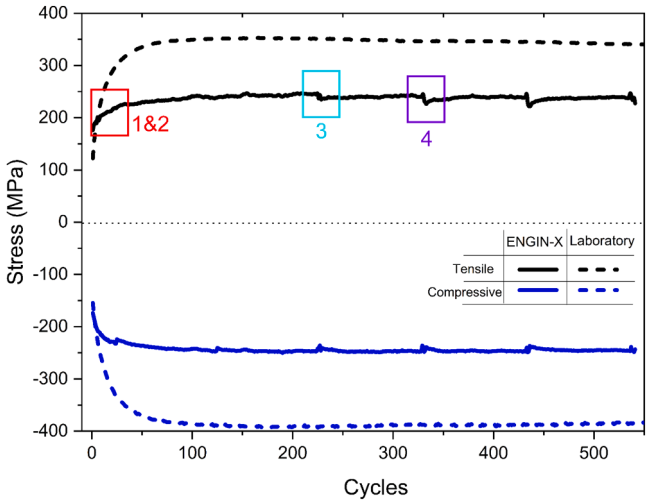

Fig. B1. Applied stress history for neutron diffraction measurement at ENGIN-X, compared to the fatigue F-S test at laboratory. Numeric labels 1 to 4 indicate the four major experimental modules.

The numeric labels 1 to 4 in Fig. B1 indicate 4 major modules. Each module was composed of one of the two waveforms (A and B) or their combinations, refer to Table S2. Modules 1 and 2 were taken from the cyclic hardening stage, while modules 3 to 4 were taken from the saturation stage. To shorten the transition period between the two stages, 100 fatigue cycles using a fast tension-fast compression waveform (abbreviated as Type C) were employed. This approach was also supposed to minimise the loading history effect induced by the previous asymmetric waveforms (Table S2).

Two stress-free lattice spacing measurements were made before and after the Type C waveform, without interference from any other waveform types. The difference between the two measurements resulted in lattice strains of 130, 60,120, 60, and 20 microstrains for the {111}, {200}, {220}, and {311} grain families, respectively. Therefore, the Type C waveform itself has been confirmed to introduce minimal change on lattice strain. These efforts ultimately allowed us to provide an objective assessment of the micro-mechanical response during the peak stress dwell after the material had experienced asymmetric load waveforms.

Data availability

Data will be made available on request.

References

Ainsworth, R.A., 2006. R5 procedures for assessing structural integrity of components under creep and creep-fatigue conditions. Int. Mater. Rev. 51, 107–126.
Anahid, M., Samal, M.K., Ghosh, S., 2011. Dwell fatigue crack nucleation model based on crystal plasticity finite element simulations of polycrystalline titanium alloys. J. Mech. Phys. Solids 59, 2157–2176.
Arsenlis, A., Parks, D.M., 1999. Crystallographic aspects of geometrically-necessary and statistically-stored dislocation density. Acta Mater. 47, 1597–1611.
Ashby, M., Dyson, B., 1984. Creep damage mechanics and micromechanisms. In: Fracture 84. Elsevier, pp. 3–30.
Ashby, M.F., 1970. The deformation of plastically non-homogeneous materials. Philos. Mag. 21, 399–424.
Benzing, J.T., Liu, Y., Zhang, X., Luecke, W.E., Ponge, D., Dutta, A., Oskay, C., Raabe, D., Wittig, J.E., 2019. Experimental and numerical study of mechanical properties of multi-phase medium-Mn TWIP-TRIP steel: Influences of strain rate and phase constituents. Acta Mater. 177, 250–265.
Betten, J., 2008. Creep Mechanics. Springer Science & Business Media.
Bhanu Sankara Rao, K., Sandhya, R., Mannan, S.L., 1993. Creep-fatigue interaction behaviour of type 308 stainless steel weld metal and type 304 stainless steel base metal. Int. J. Fatigue 15, 221–229.
Brinkman, C., Korth, G., Hobbins, R.J.N.T., 1972. Estimates of creep-fatigue interaction in irradiated and unirradiated austenitic stainless steels. Nucl. Technol. 16, 297–307.
BS 7270:2006, 2006. Metallic Materials. Constant Amplitude Strain Controlled Axial Fatigue. BSI.
Chen, B., Hu, J.N., Flewitt, P.E.J., Smith, D.J., Cocks, A.C.F., Zhang, S.Y., 2014. Quantifying internal stress and internal resistance associated with thermal ageing and creep in a polycrystalline material. Acta Mater. 67, 207–219.
Chen, B., Hu, J.N., Wang, Y.Q., Kabra, S., Cocks, A.C.F., Smith, D.J., Flewitt, P.E.J., 2015a. Internal strains between grains during creep deformation of an austenitic stainless steel. J. Mater. Sci. 50, 5809–5816.
Chen, B., Hu, J.N., Wang, Y.Q., Zhang, S.Y., Van Petegem, S., Cocks, A.C.F., Smith, D.J., Flewitt, P.E.J., 2015b. Role of the misfit stress between grains in the Bauschinger effect for a polycrystalline material. Acta Mater. 85, 229–242.
Clausen, B., Lorentzen, T., Bourke, M.A.M., Daymond, M.R., 1999. Lattice strain evolution during uniaxial tensile loading of stainless steel. Mater. Sci. Eng. A 259, 17–24.
Clausen, B., Lorentzen, T., Leffers, T., 1998. Self-consistent modelling of the plastic deformation of F.C.C. polycrstals and its implications for diffraction measurements of internal stresses. Acta Mater. 46, 3087–3098.
Coffin Jr, L.F., 1954. A study of the effects of cyclic thermal stresses on a ductile metal. Trans. Am. Soc. Mech. Eng. 76, 931–949.
Colin, J., Fatemi, A., Taheri, S., 2010. Fatigue behavior of stainless steel 304L including strain hardening, prestraining, and mean stress effects. J. Eng. Mater. Technol. 132, 021008.

Cottrell, A.H., Dexter, D.L., 1954. Dislocations and plastic flow in crystals. Am. J. Phys. 22, 242–243.
Daymond, M.R., Bouchard, P.J., 2006. Elastoplastic deformation of 316 stainless steel under tensile loading at elevated temperatures. Metall. Mater. Trans. A 37, 1863–1873.
Diercks, D., Raske, D., 1976. Elevated-temperature, Strain-Controlled Fatigue Data on Type 304 Stainless Steel. A Compilation, Multiple Linear Regression Model, and Statistical Analysis. Oak Ridge Y-12 Plant (Y-12).
Dunne, F.P.E., Rugg, D., Walker, A., 2007. Lengthscale-dependent, elastically anisotropic, physically-based hcp crystal plasticity: application to cold-dwell fatigue in Ti alloys. Int. J. Plast. 23, 1061–1083.
Estrin, Y., Mecking, H., 1984. A unified phenomenological description of work hardening and creep based on one-parameter models. Acta Metall. 32, 57–70.
Goodall, I.W., Hales, R., Walters, D.J., 1981. On constitutive relations and failure criteria of an austenitic steel under cyclic loading at elevated temperature. In: Ponter, A.R.S., Hayhurst, D.R. (Eds.), Creep in Structures. Springer Berlin Heidelberg, Berlin, Heidelberg, pp. 103–127.
Hales, R., 1980. A quantitative metallographic assessment of structural degradation of type 316 stainless steel during creep-fatigue. Fatigue Fract. Eng. Mater. Struct. 3, 339–356.
Hormozi, R., Biglari, F., Nikbin, K., 2015. Experimental and numerical creep–fatigue study of Type 316 stainless steel failure under high temperature LCF loading condition with different hold time. Eng. Fract. Mech. 141, 19–43.
Hu, C., Xu, L., Zhao, L., Han, Y., Song, K., Luo, X., Li, C., 2023. Investigation of low cycle fatigue crack propagation behavior of 316H steel at 550℃ based on cyclic response and damage accumulation: experiment and modelling. Int. J. Plast. 167, 103661.
Hu, J., Chen, B., Smith, D.J., Flewitt, P.E.J., Cocks, A.C.F., 2015. Self-consistent modelling and the evaluation of lattice deformation in a polycrystalline austenitic stainless steel. Mater. Today Proc. 2, S424–S433.
Hu, J., Cocks, A.C.F., 2016. A multi-scale self-consistent model describing the lattice deformation in austenitic stainless steels. Int. J. Solids Struct. 78–79, 21–37.
Hu, J., Liu, C., Xuan, F., Chen, B., 2022. Modeling of cavity nucleation, early-stage growth, and sintering in polycrystal under creep–fatigue interaction. Fatigue Fract. Eng. Mater. Struct. 45, 882–903.
Hu, J.D., Xuan, F.Z., Liu, C.J., Chen, B., 2021. Modelling of cavity nucleation under creep-fatigue interaction. Mech. Mater. 156, 104195.
Hyde, C.J., Sun, W., Leen, S.B., 2010. Cyclic thermo-mechanical material modelling and testing of 316 stainless steel. Int. J. Pressure Vessels Piping 87, 365–372.
Kachanov, L.M., 1999. Rupture time under creep conditions. Int. J. Fract. 97, 11–18.
Kocks, U.F., Mecking, H., 2003. Physics and phenomenology of strain hardening: The FCC case. Prog. Mater. Sci. 48, 171–273.
Lee, S.R., Lee, H.J., Chung, J.O., Oh, S.-W., Huh, C.-W., Yoon, D.-P., 1991. Waveform effect on the low cycle fatigue behavior of AISI 304 stainless steel at high temperature. Key Eng. Mater. 51–52, 1–6.
Li, D.-F., Barrett, R.A., O'Donoghue, P.E., O'Dowd, N.P., Leen, S.B., 2017. A multi-scale crystal plasticity model for cyclic plasticity and low-cycle fatigue in a precipitate-strengthened steel at elevated temperature. J. Mech. Phys. Solids 101, 44–62.
Li, R., Wang, Y.-D., Liu, W., Geng, C., Xie, Q., Brown, D.E., An, K., 2019. Multiscale mechanical fatigue damage of stainless steel investigated by neutron diffraction and X-ray microdiffraction. Acta Mater. 165, 336–345.
Li, X., Holdsworth, S.R., Kalácska, S., Balogh, L., Park, J.S., Dasilva, Y.A.R., Maeder, X., Cocks, A., Mazza, E., Hosseini, E., 2021. In-situ and ex-situ microstructure studies and dislocation-based modelling for primary creep regeneration response of 316H stainless steel. Acta Mater. 216, 117130.
Liang, F., Zhang, W., Chen, F., Yin, P., Yang, Q., Chang, L., Zhou, C., 2023. Experimental and constitutive modelling studies of type 316L stainless steel based on internal stress under low cycle fatigue and creep-fatigue interaction. Int. J. Fatigue 175, 107835.
Liu, Y., Chamaa, S.E., Wenman, M.R., Davies, C.M., Dunne, F.P.E., 2021. Hydrogen concentration and hydrides in Zircaloy-4 during cyclic thermomechanical loading. Acta Mater. 221, 117368.
Liu, Y., Wan, W., Dunne, F.P.E., 2022. Characterisation and modelling of micro- and macroscale creep and strain rate sensitivity in Zircaloy-4. Mater. Sci. Eng. A 840, 142981.
Lu, J., Sun, W., Becker, A., 2016. Material characterisation and finite element modelling of cyclic plasticity behaviour for 304 stainless steel using a crystal plasticity model. Int. J. Mech. Sci. 105, 315–329.
Lu, X., Zhang, X., Shi, M., Roters, F., Kang, G., Raabe, D., 2019. Dislocation mechanism based size-dependent crystal plasticity modeling and simulation of gradient nano-grained copper. Int. J. Plast. 113, 52–73.
Mamun, A.A., Moat, R.J., Kelleher, J., Bouchard, P.J., 2019a. The effect of cyclic-loading generated intergranular strains on the creep deformation of a polycrystalline material. Materialia 7, 100385.
Mamun, A.A., Simpson, C., Agius, D., Lee, T.L., Kabra, S., Truman, C., Mostafavi, M., Knowles, D., 2020. A novel insight into the primary creep regeneration behaviour of a polycrystalline material at high-temperature using in-situ neutron diffraction. Mater. Sci. Eng. A 786, 139374.
Mamun, A.A., Simpson, C., Erinosho, T., Agius, D., Reinhard, C., Mostafavi, M., Knowles, D., 2019b. Effect of plasticity on creep deformation in Type 316H stainless steel. In: ASME 2019 Pressure Vessels & Piping Conference. American Society of Mechanical Engineers. V06AT06A036.
Manson, S.S., 1953. Behavior of Materials Under Conditions of Thermal Stress. National Advisory Committee for Aeronautics.
May, D.L., Gordon, A.P., Segletes, D.S., 2013. The application of the Norton-Bailey law for creep prediction through power law regression. In: ASME Turbo Expo 2013, GT2013-95405.
Mecking, H., Kocks, U.F., 1981. Kinetics of flow and strain-hardening. Acta Metall. 29, 1865–1875.
Muránsky, O., Balogh, L., Tran, M., Hamelin, C.J., Park, J.S., Daymond, M.R., 2019. On the measurement of dislocations and dislocation substructures using EBSD and HRSD techniques. Acta Mater. 175, 297–313.
Oh, C.-S., Kim, N.-H., Kim, Y.-J., Davies, C., Nikbin, K., Dean, D., 2011. Creep failure simulations of 316H at 550°C: Part I – a method and validation. Eng. Fract. Mech. 78, 2966–2977.
Okazaki, M., Hattori, I., Koizumi, T., 1984. The effect of one slow-fast strain cycle on the fatigue crack growth behavior of SUS 304 stainless steel at elevated temperature. Metall. Trans. A 15, 1731–1739.
Pai, N., Samajdar, I., Patra, A., 2025. Study of orientation-dependent residual strains during tensile and cyclic deformation of an austenitic stainless steel. Int. J. Plast. 185, 104228.
Peng, R.L., Odén, M., Wang, Y.D., Johansson, S., 2002. Intergranular strains and plastic deformation of an austenitic stainless steel. Mater. Sci. Eng. A 334, 215–222.
Petkov, M.P., Elmukashfi, E., Cocks, A.C.F., 2022. Multi-scale modelling of creep cavity nucleation and growth in polycrystalline Type 316 stainless steel. Philos. Mag. 102, 2362–2411.
Petkov, M.P., Hu, J., Tarleton, E., Cocks, A.C.F., 2019. Comparison of self-consistent and crystal plasticity FE approaches for modelling the high-temperature deformation of 316H austenitic stainless steel. Int. J. Solids Struct. 171, 54–80.
Podesta, L., Wattrisse, B., Latourte, F., Waltz, L., Muracciole, J.M., 2017. In-situ tensile test on 316H sent using digital image correlation. In: Zhu, Y., Zehnder, A.T. (Eds.), Experimental and Applied Mechanics, Experimental and Applied Mechanics, 4. Springer International Publishing, Cham, pp. 45–52.
Pokharel, R., Patra, A., Brown, D.W., Clausen, B., Vogel, S.C., Gray, G.T., 2019. An analysis of phase stresses in additively manufactured 304L stainless steel using neutron diffraction measurements and crystal plasticity finite element simulations. Int. J. Plast. 121, 201–217.
Prasad Reddy, G.V., Kannan, R., Mariappan, K., Sandhya, R., Sankaran, S., Bhanu Sankara Rao, K., 2015a. Effect of strain rate on low cycle fatigue of 316LN stainless steel with varying nitrogen content: Part-I cyclic deformation behavior. Int. J. Fatigue 81, 299–308.
Prasad Reddy, G.V., Sandhya, R., Sankaran, S., Parameswaran, P., Laha, K., 2015b. Creep–fatigue interaction behavior of 316LN austenitic stainless steel with varying nitrogen content. Mater. Des. 88, 972–982.
Rao, A., John Bouchard, P., Northover, S.M., Fitzpatrick, M.E., 2012. Anelasticity in austenitic stainless steel. Acta Mater. 60, 6851–6861.
Roters, F., Eisenlohr, P., Hantcherli, L., Tjahjanto, D.D., Bieler, T.R., Raabe, D., 2010. Overview of constitutive laws, kinematics, homogenization and multiscale methods in crystal plasticity finite-element modeling: theory, experiments, applications. Acta Mater. 58, 1152–1211.
Sauzay, M., Mottot, M., Allais, L., Noblecourt, M., Monnet, I., Périnet, J., 2004. Creep-fatigue behaviour of an AISI stainless steel at 550°C. Nucl. Eng. Des. 232, 219–236.

Skelton, R., Gandy, D., 2008. Creep–fatigue damage accumulation and interaction diagram based on metallographic interpretation of mechanisms. Mater. High Temp. 25, 27–54.
Spindler, M.W., Payten, W., 2011. Advanced ductility exhaustion methods for the calculation of creep damage during creep-fatigue cycling. Creep-Fatigue Interactions: Test Methods and Models.
Spindler, M.W., 2004. The multiaxial creep ductility of austenitic stainless steels. Fatigue Fract. Eng. Mater. Struct. 27, 273–281.
Spindler, M.W., 2005. The prediction of creep damage in type 347 weld metal. Part I: the determination of material properties from creep and tensile tests. Int. J. Press. Vessels Pip. 82, 175–184.
Spindler, M.W., 2018. Creep-fatigue endurance of Type 316H parent cast 69431. EDF Energy Nucl. Gener. Ltd.
Srinivasan, V.S., Valsan, M., Sandhya, R., Bhanu Sankara Rao, K., Mannan, S.L., Sastry, D.H., 1999. High temperature time-dependent low cycle fatigue behaviour of a type 316L(N) stainless steel. Int. J. Fatigue 21, 11–21.
Taira, S., 1962. Lifetime of structures subjected to varying load and temperature. Creep in Structures: Colloquium Held at Stanford University, California July 11–15, 1960. Springer, pp. 96–124.
Takahashi, Y., 2008. Study on creep-fatigue evaluation procedures for high-chromium steels—Part I: test results and life prediction based on measured stress relaxation. Int. J. Press. Vessels Pip. 85, 406–422.
Takahashi, Y., Shibamoto, H., Inoue, K., 2008. Study on creep-fatigue life prediction methods for low-carbon nitrogen-controlled 316 stainless steel (316FR). Nucl. Eng. Des. 238, 322–335.
Taylor, G.I., 1997. The mechanism of plastic deformation of crystals. Part II.—comparison with observations. Proc. R. Soc. Lond. Ser. A, Contain. Pap. Math. Phys. Character 145, 388–404.
Wang, H., Clausen, B., Tomé, C.N., Wu, P.D., 2013. Studying the effect of stress relaxation and creep on lattice strain evolution of stainless steel under tension. Acta Mater. 61, 1179–1188.
Wang, R.-Z., Guo, S.-J., Chen, H., Wen, J.-F., Zhang, X.-C., Tu, S.-T., 2019. Multi-axial creep-fatigue life prediction considering history-dependent damage evolution: a new numerical procedure and experimental validation. J. Mech. Phys. Solids 131, 313–336.
Wang, Y.Q., Kabra, S., Zhang, S.Y., Truman, C.E., Smith, D.J., 2018. An in situ thermo-mechanical rig for lattice strain measurement during creep using neutron diffraction. Rev. Sci. Instrum. 89, 055110.
Wen, J.-F., Srivastava, A., Benzerga, A., Tu, S.-T., Needleman, A., 2017. Creep crack growth by grain boundary cavitation under monotonic and cyclic loading. J. Mech. Phys. Solids 108, 68–84.
Wen, J.-F., Tu, S.-T., Xuan, F.-Z., Zhang, X.-W., Gao, X.-L., 2016. Effects of stress level and stress state on creep ductility: evaluation of different models. J. Mater. Sci. Technol. 32, 695–704.
Xie, X.f., Jiang, W., Chen, J., Zhang, X., Tu, S.T., 2019. Cyclic hardening/softening behavior of 316L stainless steel at elevated temperature including strain-rate and strain-range dependence: experimental and damage-coupled constitutive modeling. Int. J. Plast. 114, 196–214.
Yamaguchi, K., Kanazawa, K., 1980. Effect of strain wave shape on high temperature fatigue life of a type 316 steel and application of the strain range partitioning method. Metall. Trans. A 11, 2019–2027.
Zepeda-Ruiz, L.A., Stukowski, A., Oppelstrup, T., Bulatov, V.V., 2017. Probing the limits of metal plasticity with molecular dynamics simulations. Nature 550, 492–495.
Zhang, Z., Jun, T.-S., Britton, T.B., Dunne, F.P.E., 2016. Determination of Ti-6242 α and β slip properties using micro-pillar test and computational crystal plasticity. J. Mech. Phys. Solids 95, 393–410.